Late Permian–Middle Triassic magnetostratigraphy in North China and its implications for terrestrial-marine correlations

Wenwei Guo[a], Jinnan Tong[a, *], Qi He[b], Mark W. Hounslow[c, d], Huyue Song[a], Jacopo Dal Corso[a], Paul B. Wignall[e], Jahandar Ramezani[f], Li Tian[a], Daoliang Chu[a]

[a]*State Key Laboratory of Biogeology and Environmental Geology, School of Earth Science, China University of Geosciences, Wuhan 430074, China*

[b]*State Key Laboratory of Geological Processes and Mineral Resources, Planetary Science Institute, School of Earth Sciences, China University of Geosciences, Wuhan 430074, China*

[c]*Lancaster Environment Centre, Lancaster University, Lancaster, UK*

[d]*Earth, Ocean and Ecological Sciences, University of Liverpool, Liverpool, Jane Herdman Building, UK*

[e]*School of Earth and Environment, University of Leeds, Leeds, UK*

[f] *Department of Earth, Atmospheric and Planetary Sciences, Massachusetts Institute of Technology, Cambridge, MA 02139, USA*

**Corresponding author*: jntong@cug.edu.cn (J.N. Tong)

Abstract

A detailed magnetostratigraphic study, tied to a new latest Permian U–Pb ID-TIMS radioisotopic age from an ash bed, was carried out from the continental Shichuanhe section in North China in order to provide a magnetic polarity scale from the Late Permian–early Middle Triassic. The tilt-corrected mean directions of the characteristic remanent magnetization pass the reversal test and correspond to a site paleolatitude of 18.1°N during the Early Triassic, consistent with previous results from the North China Block. The magnetostratigraphy shows excellent similarity with previous studies, allowing interregional correlations to other marine and non-marine records. Normal magnetozone SCH3n, constrained by an absolute age of 252.21±0.15 Ma from 3.5 m below its base, is unambiguously correlated to the earliest Triassic normal magnetochron LT1n. This newly established magnetostratigraphic framework and published carbon-isotope chemostratigraphy indicate the Permian–Triassic Boundary (PTB) is ca. 8 m above the base of SCH3n (within the middle part of the Sunjiagou Formation) and additionally demonstrates a continuous PTB sequence at SCH. The overlying reverse polarity dominated interval (SCH3r–SCH5r) to the middle Liujiagou Formation, straddles an interval from the mid-Griesbachian to mid-Smithian. The base of the Olenekian is provisionally located in the lower part of the Liujiagou Formation, near the base of magnetozone SCH5n. The succeeding thick normal magnetozone SCH6n persist into the upper Heshanggou Formation, with the inferred Smithian–Spathian boundary in the upper part of the Liujiagou Formation. The transition from reverse magnetozone SCH6r to the overlying normal magnetozone SCH7n, coincides with a clear erosional contact with the base of the Emaying Formation. Consequently, magnetozone SCH7n is matched to the Early Anisian magnetochron MT3n, with the Olenekian–Anisian boundary interval missing. Our new integrative timescale also provides additional magnetostratigraphic constraints on the terrestrial ecological crisis in North China, which lies within reverse magnetozone SCH2r, some 270±150 kyrs before the main marine extinction, that falls in the overlying normal magnetochron LT1n, as confirmed by the radioisotopic date.

Key words: Magnetostratigraphy, marine-terrestrial correlation, ID-TIMS age, terrestrial extinction

1. Introduction

The Late Permian–Middle Triassic is a key interval in the history of life, which is marked by the most severe extinction of the Phanerozoic, i.e., the Permian–Triassic mass extinction (PTME) at about 252 Ma (Wignall, 2015; Benton, 2018). Persistent environmental perturbations followed throughout the Early Triassic (Payne et al., 2004; Song et al., 2012; Sun et al., 2012; Wu et al., 2021b), resulting in a protracted biotic recovery for more than 5 Ma after the PTME (Chen and Benton, 2012), although marine ecosystem recovery was still underway in the latest Triassic (Song et al., 2018). Notably, knowledge about the timing, magnitude and duration of the PTME and its aftermath are largely derived from marine records because they are stratigraphically most complete, can be more easily correlated using biostratigraphy and are better constrained by absolute ages (Chen and Benton, 2012; Burgess et al., 2014).

In contrast, a full understanding of the PTME and its following biotic restoration on land is more challenging, due to the more varied depositional environments, probably less-continuous sedimentary record, and typically rather poorly age constrained. Recently, increasing studies have shed light on the timing of the terrestrial ecological crisis, which have argued for extinction on land preceding that in the oceans by about 50 kyr to 240–640 kyr, with differing paces among continental basins (Fielding et al., 2019, 2021; Chu et al., 2020; Gastaldo et al., 2020). Although knowledge about the PTME in terrestrial facies have improved, the relative timing of biological recovery on land cannot be easily compiled because a globally unified fine-scale chronostratigraphy is not available. Causal links between unusual sedimentary structures, such as microbial mats and possible hurricanes, during the Early Triassic linked to abnormal environmental conditions are also challenging to understand (Chu et al., 2015, 2017; Ji et al., 2021). Therefore, a more integrative approach that allows events to be temporally constrained throughout the Early Triassic, using tool such as magnetostratigraphy, is required for a better appreciation of the global ecological evolution.

The global and synchronous nature of geomagnetic polarity boundaries has made magnetostratigraphy an important approach for precise correlation between successions, a tool which is independent of facies control. In the last two decades, significant progress has been achieved in establishing a comprehensive time-calibrated magnetostratigraphy during the Permian and Triassic, that provides a scale for interregional correlations (e.g., Steiner, 2006; Hounslow and Muttoni, 2010; Hounslow and Balabanov, 2018). Reliable PTB magnetostratigraphies have also been constructed in continental successions, including in Europe and eastern Australia (Szurlies, 2003; Szurlies et al., 2013; Belica, 2017), but a detailed continental-succession based magnetic stratigraphy through the entire Early Triassic is only available in the Central European Basin (Szurlies, 2007). However, magnetostratigraphy in North China, straddling the complete Late Permian to Middle Triassic has been rarely undertaken and a detailed regional polarity reversal pattern is difficult to unravel owing to the coarse spatial sampling and lack of specific correlation anchors (e.g., using biostratigraphy, radioisotopic ages). Thus, regional lithostratigraphic templates have been widely used (Ma et al., 1992; Embleton et al., 1993).

We present a high resolution magnetostratigraphy from the Upper Permian throughout the Lower Triassic to the earliest Anisian (Middle Triassic) in central North China. A new U-Pb CA-ID-TIMS (chemical abrasion isotope dilution thermal ionization mass spectrometry) age from an ash bed within the middle part of the Sunjiagou Formation provides a geochronological anchor for the new magnetostratigraphic framework. Coupled to available biostratigraphy and carbon-isotope chemostratigraphy, our multi-disciplinary approach enables establishment of a detailed timescale on land from Late Permian–earliest Middle Triassic in North China, which locates the PTB at the Shichuanhe (SCH) section, and so understand the relative timing between the terrestrial PTME and marine extinctions.

2. Geological setting

The Ordos Basin was a large depocenter that formed part of the intracratonic central North China Basin, located at 10–20°N paleolatitude during the Paleozoic–Mesozoic transition, which was bordered by the Liupan-Helan-Yin-Lvliang uplands to the west and southeast and passed into further terrestrial basins to the northeast (Huang et al., 2018; Meng et al., 2019; Fig. 1A). Since cratonization, the Early Cambrian deposits in the North China Block were followed by a major hiatus in the Middle Ordovician to the Mississippian due to regional uplift. Sedimentation resumed after a major transgression in the Pennsylvanian, represented by alternating marine and terrestrial sequences with well-developed coals (Yang et al., 2017). During the Permian the North China block was largely comprised of terrestrial systems, in which coal forming environments ceased in the upper Shihhotse Formation in the Early Permian, according to ID-TIMS dating (Wu et al., 2021a). The Permian–Triassic Shiqianfeng Group is characterized by red beds, which contains rare body fossils that are inadequate to establish a detailed biostratigraphy (Tong et al., 2019). This interval is also poorly dated apart from two LA-ICP-MS ages obtained from detrital zircons (Zhu et al., 2019; Fig. 1C). However, a mixed terrestrial spinicaudatan-marine bivalve assemblage, a consequence of a regional marine transgression in the southern Ordos Basin, allows identification of the Permian–Triassic transitional beds at SCH (Chu et al., 2019).

The Shiqianfeng Group is divided from base to top into the Sunjiagou, Liujiagou and Heshanggou formations, which are overlain by the Ermaying Formation (Fig. 1C). The Sunjiagou Formation consists of green sandstone with interbedded mudstone in the lower part, containing a Late Permian *Ullmannia bronnii-Pseudovoltzia* cf. *libeana* flora assemblage (Lu et al., 2020), representing deposition in fluvial channels and point bars (Zhu et al., 2019, 2020). However, this unit is not well exposed at SCH and thus, the nature of the boundary with the underlying strata is unclear. The overlying portion is characterized by a color change to a sequence of dominantly red siltstones, with well-developed paleosols that formed on a floodplain (Zhu et al., 2020). This is followed by alternating thin, fine-grained sandstones, massive mudstones and marlstones, with rare ripple marks, and desiccation cracks, interpreted as the deposits of a coastal facies with occasional drying (Yu et al., 2022; Ji et al., under review). The time interval covered by the Sunjiagou Formation is controversial, with the supposed PTB, defined by tetrapods, organic carbon isotopes and mixed marine-terrestrial biota, having a position postulated to range from the mid to the top of the Sunjiagou Formation (Chu et al., 2019; Zhu et al., 2019, 2020; Lu et al., 2020; Wu et al., 2020).

The mud-rich floodplain and coastal facies of the Sunjiagou Formation were interrupted by a pronounced change to the fluvial-dominated, sandstone-rich Liujiagou Formation (Zhu et al., 2020; Ji et al., 2021). Conglomeratic intraclasts, concentrically-laminated concretions and microbial mats are found within the interlayered lacustrine facies of the Liujiagou Formation (Chu et al., 2015, 2017; Ji et al., 2021). Aeolian deposits are also reported from the northern part of the basin (Zhu et al., 2020). The Liujiagou Formation contains very rare fossils, with plants attributed to the *Pleuromeia jiaochengensis* assemblage in the middle to upper parts (Wang and Wang, 1990). The base of the Liujiagou Formation has traditionally been considered conformable, although a disconformity has also been suggested (IGCAGS, 1980).

The overlying Heshanggou Formation is marked by a return to dominantly dark red mudstones and siltstones, which rest conformably on the underlying strata. Laterally persistent sandstones become dominant upwards, and primary sedimentary structures are hard to detect due to well-developed paleosols and bioturbation throughout the formation (Guo et al., 2019; Yu et al., 2022). The fluvial overbank and shallow lacustrine facies interpreted for the Heshanggou Formation (Zhu et al., 2020) contain diverse fossils (e.g., vertebrates, ostracods and sporomorphs), which are indicative of the late Early Triassic (IGCAGS, 1980).

The succeeding Ermaying Formation is characterized by massive green fluvial sandstones with interbedded green and red mudstones and conglomerates, which probably rest conformably on the underlying strata (IGCAGS, 1980). However, the basal sandstones of the Ermaying Formation at SCH contain imbricated conglomerates and large mud clasts, implying a basal erosional contact, suggestive of a possible local hiatus (Supplementary Fig. S1). The *Parakannemeyeria* fauna and an Anisian U-Pb ID-TIMS age of 243.528±0.069 Ma suggest the Ermaying Formation is Middle Triassic in age (Liu et al., 2018).

3. Materials and methods

3.1 Paleomagnetic methods and analysis

Magnetostratigraphic, sedimentological and geochronological analyses were undertaken at the Shichuanhe section (GPS: 35.03°N, 108.88°E), located near Tongchuan, 90 km north of Xi'an City, Shaanxi Province. Magnetostratigraphic samples were collected throughout the section, using both hand samples, oriented in situ by a magnetic compass, and oriented core-plugs made by a portable field drill. In total, 272 hand samples from fine-grained sediments and marlstones, and 39 core plugs from sandstones, were collected, covering an interval spanning the inferred Late Permian to basal Middle Triassic (Supplementary Fig. S2). Sample spacing ranges from 0.5 to 2.5 m, depending on suitable lithologies. In the laboratory, 56 hand samples were excluded from paleomagnetic studies because they were too fractured and could not be prepared into specimens. Each of the remaining samples was cut into at least two 2 cm cubes or 2 cm long cylinders for paleomagnetic measurements.

All specimens were subjected to stepwise thermal demagnetization using 16–19 steps (up to 680°C) in a Magnetic Measurements ASC TD48 thermal specimen demagnetizer. Each heating was followed by cooling in a residual magnetic field ≤20 nT. Specimens were housed in a magnetically shield room with ambient magnetic field ≤300 nT and measured on a 2G Enterprises 755-4K U-Channel magnetometer at the China University of Geosciences (Wuhan), China. Characteristic remanent magnetization directions (ChRMs) were isolated using principal component analysis, as implemented in the PuffinPlot software (Lurcock and Wilson, 2012). Both linear trajectory fits and great circles (remagnetization circles) were used in defining the paleomagnetic behaviors. The PMAGTOOL v5. software (Hounslow, 2006) was also used for calculation of mean directions, virtual geomagnetic poles (VGP) and performing the reversal tests. The ChRM directions isolated were classified into different categories based on their demagnetization behavior and quality, similar to the method of Hounslow et al. (2008). ChRMs displaying clear linearity or exhibiting great-circle trends were categorized into S-type or T-type behaviors, respectively. For S-type data, specimens were subdivided into three quality levels (S1, S2 and S3) based on the visual noisiness and length of colinear points, with S1 showing best quality and S3 the lowest quality. T-type data were also reclassified into three levels (T1, T2 and T3) according to the visual length and scatter of the demagnetization points about the great circle, with T1 having the best-quality great circle trend, which terminated near the expected Triassic direction, and T3 for the poorer results. Specimen demagnetization results were interpreted with a polarity quality rating on the basis of a semi-subjective judgment (e.g., for normal polarity, N=best quality, N?=intermediate quality and N?? =poorest quality). Specimens without an interpreted Permian–Triassic magnetizations are labelled as X quality. Poorer quality data (e.g., S3 and T3 demagnetization behaviors) were not used for mean direction calculations, but were used for VGP latitude calculations.

Representative specimens from green and red lithologies were selected to determine the main magnetic remanence carriers using magnetic susceptibility versus temperature experiments (K-T curves). Specimens were heated up to 700°C in air at 10°C/min, and subsequently cooled at the same rate to room temperature. The K-T curves were measured using an AGICO, MFK1-FA Kappabridge, at the China University of Geosciences (Wuhan).

3.2 U-Pb geochronology

Zircons were separated from a ~1 cm thick ash bed in the middle part of the Sunjiagou Formation at SCH. Forty extracted zircons were subjected to U-Pb LA-ICP-MS (Laser Ablation Inductively Coupled Plasma Mass Spectrometry) at the Mineral Rock Laboratory, Hubei Province Geological Experimental Testing Center, before being analyzed by the U-Pb CA-ID-TIMS method at the Massachusetts Institute of Technology (MIT) Isotope Laboratory, USA. General analytical procedures of the ID-TIMS experiment are described in Ramezani et al. (2011). Detailed U-Pb methods are provided in Supplementary Data A. Seven chemically abraded zircons were spiked with the EARTHTIME ET535 mixed U-Pb tracer before complete dissolution in HF, purification of Pb and U by column chemistry and measurement of the Pb and U isotopes on the mass spectrometer.

Complete LA-ICP-MS results and U-Pb isotopic data are given in Supplementary Data C. The weighted mean age uncertainty of ID-TIMS is reported at 95% confidence interval and in the format ±x/y/z Ma, where x is the analytical (internal) uncertainty only, y includes the additional tracer calibration error and z includes the latter as well as the 238U decay constant error of Jaffey et al. (1971).

4. Results

4.1 Rock magnetism

Susceptibility of most of the red specimens consistently reduces at around 700°C, which is attributed to hematite. One sample exhibits a large rise in susceptibility at 450°C (from thermal alteration), but subsequently decreases at 585°C and 680°C, suggesting the presence of both magnetite and hematite. The susceptibility of green lithologies generally show curve inflexions at around 585°C, corresponding to the Curie temperature of magnetite. Therefore, magnetite and hematite appear to be the main magnetic remanence carriers of the magnetization in green and red sediments, respectively (Supplementary Fig. S4). A decline in susceptibility below 100°C in many samples may be due to goethite. The magnetization carriers are consistent with the thermal demagnetization behavior of the natural remanent magnetization (NRM) and previous investigations (Yang et al., 1991).

4.2 U-Pb geochronology

Fifteen grains from forty zircons analyzed by LA-ICP-MS, with a high concordance, yield ages of

263±2.7 Ma to 249±2.5 Ma, and nine grains display ages that cover the PTB (Supplementary Fig. S5 and Supplementary data C). Five chemically abraded single zircon grains yielded overlapping 206Pb/238U dates, with a weighted mean of 252.21±0.15 Ma and a mean square of weighted deviates (MSWD) of 0.45 (Fig. 5). But one analysis produced a significantly younger Jurassic age, which are in conflict with regional sediment sources and LA-ICP-MS results, and thus was rejected (See Supplementary Data A for discussion). The weighted mean date is the best estimate for the (maximum) age of deposition of the corresponding ash bed.

4.3 Paleomagnetic properties

Commonly, the untreated NRM intensities range between 0.1–10 mA/m, with a few exceptions up to 30 mA/m (Fig. 4 and Supplementary Fig. S3). There was considerable variation in demagnetization behavior between different lithologies. But usually, specimens showed two components, a low-temperature component (LTC) and a high-temperature component (HTC), which could be isolated during thermal demagnetization. More details about the demagnetization behavior and polarity interpretations are in Supplementary files A and B.

(a) A LTC was obtained in most specimens, which generally unblocked between NRM to ca. 200–450°C (Fig. 2B–2E, 2H–2I). This LTC is generally northerly directed with a relatively steep inclination in geographic coordinates (Fisher mean of D=355.4°, I=55.3°, $\alpha95$=5.1°, n=244; Fig. 3A). The direction is comparable to the present-day field at the site (D=355.9°, I=54.1°, World Magnetic Model 2019–2024), which is inferred to be a recently acquired or more likely a Brunhes-age overprint.

(b) The HTC is isolated by both line fit and great circle fit (Fig. 2). Red and sometimes green colored sediments fully demagnetized at 600–680°C, indicating hematite is the main carrier of the NRM (Fig. 2A–2E). A third of the greenish specimens became directionally erratic above 600°C, suggesting hematite is less important in these specimens (Fig. 2H). Some 55% of specimens display stable endpoints with a linear segment towards the origin in orthogonal projections (i.e., S-type; Fig. 2A–2F), and 87% of line-fit results yield acceptable quality (S1and S2) that could be used in a mean direction calculation (see Supplementary Table S1 for details). After tilt correction the mean normal-polarity HTC direction is concentrated in the NW with shallow positive inclination (D=325.0°, I=34.0°, α_{95}=2.9°, n=93), and the mean reverse-polarity HTC direction is D=146.4°, I=-28.5°, (α_{95}=4.9°, n=31; Fig. 3B). The site paleolatitude of all the data converted to normal polarity is 17.7°N, regardless of potential inclination shallowing produced during later compaction (Table 1). Paleomagnetic mean directions pass the reversal test with class Rb (McFadden and McElhinny, 1990). A fold test is not possible due to the shallow bedding dips in the section.

(c) For the HTC, 37% of samples yield a great circle trend toward the characteristic directions. These were used for great circle fits to determine the unresolved directions (T-type; Fig. 2G–2I). About three-quarters of the T-type data display scatter terminating at around the observed mean S-class direction. T1 and T2 quality great circles were used in the mean direction calculation. A combination of line-fit ChRM directions and great circle poles (Fig. 3C), using the method of McFadden and McElhinny (1988), gave a combined mean direction for the HTC of D=325.6°, I=33.3° (α_{95}=1.9°, n=197), corresponding to a paleopole at 55.2°N, 359.0°E (dp/dm=1.23/2.16) and site paleolatitude of 18.1°N (Table 1). The combined mean directions have a positive reversal test with class Ra (McFadden and McElhinny, 1990).

The antipodal nature of the normal- and reverse-polarity subsets (Fig. 3B) and the statistically similar directions compared to previously published Lower Triassic direction in nearby regions (Yang et al., 1991; Ma et al., 1992; Table 1), suggests that the magnetization is primary and obtained near the time of deposition.

4.4 Magnetostratigraphy

The line-fit ChRM directions were converted to virtual geomagnetic pole (VGP) latitude using the combined great circle-fixed point mean direction as the reference pole. VGP latitudes reveal the polarity changes in the section with positive/negative values indicating normal/reverse polarity (Fig. 4). For specimens that display great circle trends, the point on the fitted great circle nearest the combined mean direction was used to calculate the VGP latitude (Hounslow et al., 2008). Major magnetozone normal and reverse couplets are labelled upward from the base of the section using the prefix SCH (Shichuanhe), with polarity magnetozones pairs comprising a lower predominantly normal-polarity ("N") and an overlying reversed-polarity "R". Intervals denoted by lowest quality and poorly defined directions (e.g., S3, T3 and X), are indicated with a gray bar to display uncertainly. Seven main magnetozones, from SCH1 to SCH7, are based on at least three successive specimens with consistent polarity. Also present are a number of tentative submagnetozones (less than full width bars marked as .1r, .1n etc.), defined by a single specimen with acceptable quality (Fig. 4).

5. Discussion

5.1 Permian–Triassic boundary magnetostratigraphy in North China

The Permian–Triassic Boundary occurs in normal magnetochron LT1n, a position which has been well documented in both marine and non-marine successions (Hounslow and Balabanov, 2018 and references therein). At the Induan Global Boundary Stratotype Section and Point (GSSP) in Meishan, South China, the base of the Triassic is marked by the first occurrence (FO) of the conodont *Hindeodus parvus* in Bed 27c (Yin et al., 2001). However, magnetostratigraphic studies from Meishan display poor inter-study consistency, thus the exact relationship between the FO of *H. parvus* and the boundaries of magnetozone LT1n are unclear in the GSSP (Hounslow and Muttoni, 2010; Zhang et al., 2021). At the Shangsi section, the base of magnetochron LT1n coincides with the base of the Feixianguan Formation (base of bed 28), within the *Clarkina meishanensis* conodont zone, which was estimated at 252.23±0.08 Ma using a Monte Carlo statistical method (Yuan et al., 2019; Fig. 6 and 7). This is similar to the 252.2±0.23 Ma age for the base of LT1n estimated using Bayesian methods in Hounslow and Balabanov (2018). Hence, at the SCH section, magnetozone SCH3n is equivalent to magnetochron LT1n, based on our new age of 252.21±0.15 Ma obtained from an ash bed 3.5 m below the base of SCH3n (Fig. 6). Given the latest calibration of the PTB at 251.902±0.024 Ma based on U-Pb CA-ID-TIMS geochronology (Burgess et al., 2014), this latest Changhsingian date provides independent, radioisotopic evidence to establish a robust PTB magnetostratigraphic framework for North China. The comparative age and the polarity stratigraphy indicate that the base of LT1n is a synchronous marker useful for global correlation, occurring ca. 0.3 Ma prior to the PTB (Fig. 7).

The correlation is also supported by biostratigraphic evidence from the mixed marine-terrestrial biota found at SCH. This fauna consists of a terrestrial spinicaudatan (conchostracan) *Euestheria gutta-Magniestheria mangaliensis-Palaeolimnadiopsis vilujensis* assemblage and the marine bivalve *Pteria variabilis*, which is found about 1 m above the base of magnetozone SCH3n.

This fauna is akin to the mixed terrestrial-marine biota in South China, which appears immediately after the demise of the Late Permian *Gigantopteris* flora (Chu et al., 2019). The *Euestheria gutta* assemblage with co-preserved specific marine bivalves has also been considered an important marker for the Permian–Triassic transitional beds (Chu et al., 2019). A similar spinicaudatan fauna (*Euestheria gutta-Palaeolimnadiopsis vilujensis* assemblage) was also recognized in the lower Buntsandstein coeval with the Central German Composite magnetozone interval CG3n–4n, which is equivalent to magnetochron LT1n (Szurlies, 2007, 2013; Scholze et al., 2017; Fig. 6).

Compiled data from many marine carbonate successions have indicated that the major minimum in $\delta^{13}C_{carb}$ was around the PTB (e.g., Korte and Kozur, 2010), and falling within the lower part of LT1n (Shen et al., 2019; Zhang et al., 2021). Such carbon isotopic excursions have also been suggested to be nearly synchronous with the changes in $\delta^{13}C_{org}$ in terrestrial facies (Wu et al., 2021b). Thus, by combining the magnetostratigraphy and geochronology with the organic carbon isotope curve (Wu et al., 2020), the PTB at SCH is estimated to occur at a level about 8 m higher than the base of magnetozone SCH3n, around the largest negative excursion in $\delta^{13}C_{org}$, within the upper part of the middle Sunjiagou Formation (Fig. 7). Additionally, our new magnetostratigraphic data also allows a better constraint for the onset of the carbon isotope excursion (CIE) during the latest Permian. This was previously suggested to be located at ~27 m below the base of SCH3n on the basis of purely chemostratigraphic considerations (Wu et al., 2020), but is now placed ~3 m below the base of SCH3n, within the upper part of magnetozone SCH2r (i.e., magnetochron LP3r; Fig. 7).

Our results are also in good agreement with the age-constrained magnetostratigraphy from the Sydney Basin, eastern Australia. The Permian–Triassic transition of the Sydney Basin contains three normal magnetozones, with normal magnetozone C2n first detected in the base of the Coalcliff

Sandstone (Belica, 2017; Fig. 7). The radioisotopic ages from the basal Bulli Coal (Metcalfe et al., 2015) and basal Coalcliff Sandstone (Fielding et al., 2019, 2021) allow a robust correlation of magnetozone C2n with LT1n. However, the position of the base of magnetozone C2n is unclear, since there is a ~3.5 m unsampled interval covering the underlying Bulli Coal bed (Fig. 7).

The Permian–Triassic magnetostratigraphy from the Karoo Basin, South Africa is equivocal. The integrated magnetic polarity stratigraphy of Ward et al. (2005) showed two reverse-to-normal couplets. The longer normal magnetozone of the lower couplet, has its base slightly preceding the vertebrate turnover, with an associated negative $\delta^{13}C_{carb}$ excursion, which was suggested equivalent with magnetochron LT1n. However, this situation has not been confirmed by subsequently studies. The *Daptocephalus–Lystrosaurus* transition is mostly within a normal magnetozone (see summaries in Gastaldo et al., 2021), which is, coupled to a U-Pb ID-TIMS age of 253.48 Ma from ~60 m below the vertebrate-defined PTB and is so considered to be early Changshingian (Gastaldo et al., 2015). This inconsistency could either be due to a local hiatus (Gastaldo et al. 2015) or difficulties in isolating the primary magnetization from the Jurassic partial remagnetization (Belica, 2017).

Correlation of magnetozone interval SCH1–SCH2 to the GPTS is not straightforward due to the lack of supporting fossil markers within this interval. Also, intrabasinal correlation with the nearby Hancheng section at this level is difficult owing to the infrequent magnetostratigraphic sampling, which defines magnetozone O1 (Ma et al., 1992; Fig. 6). Overall, the relative thickness of magnetozones SCH1n–SCH2r are similar to magnetozone interval CG1n–CG2r in the Central German Composite (Szurlies, 2013; Fig. 6). In the Germanic Basin, magnetozones CG1n and CG2n were correlated to magnetozones IRA1n and IRA2n from the Abadeh section (Fig. 6), corresponding to the late Wuchiapingian and early Changhsingian on the basis of the conodonts (*Merrillina* *divergens* and *Mesogondolella britannica*) and Re-Os dating from the Zechstein successions (Szurlies, 2013; Fig. 6). However, these conodonts occur throughout the Lopingian and fail to provide a precise timescale (Henderson and Mei, 2000). Instead, magnetozone CG1n has been correlated to magnetochron LP2n.3n (equivalent to IRA2n), with its upper boundary at ca. 253.2 Ma, within the *Clarkina subcarinata* conodont zone at the Abadeh section and probably within the *C. changxingensis* zone at Shangsi (Hounslow and Balabanov, 2018). Accordingly, magnetozone SCH1n is tentatively correlated to magnetochron LP2n.3n and SCH2n to LP3n (Fig. 6).

5.2 Lower Triassic magnetostratigraphy in North China

The two reference polarity scales for the remainder of the Lower Triassic, that from Buntsandstein (Szurlies, 2007, 2013) and the marine composite GPTS (Hounslow and Muttoni, 2010), are generally similar, but show a few differences in number and relative duration of the briefer magnetochrons (Fig. 6). The placement of the Induan–Olenekian Boundary (IOB) in the Buntsandstein composite also has some divergences of interpretation (Szurlies, 2007; Hounslow and Muttoni, 2010). In China, the IOB is informally defined by the FAD of *Novispathodus waageni* s.l. at West Pingdingshan section, ~2.5 m from the top of reverse magnetozone WP4r and equivalent to the topmost part of magnetochron LT2r (Sun et al., 2009; Fig. 6). The *Densoisporites nejburgii* palynological assemblage from the Middle Buntsandstein, spans the late Dienerian to Smithian, suggesting that the IOB in Central Germany is within the lower part of the Middle Buntsandstein (Kürschner and Herngreen, 2010; Fig. 6), suggesting that CG6n is the equivalent to LT3n in the GPTS (orange correlation box in Fig. 6).

At SCH, the reverse polarity dominated interval SCH3r–SCH5r is correlated to the dominantly reverse magnetochron interval LT1r–LT4r and CG4r–CG7r, spanning the mid-Griesbachian to mid-Smithian (Fig. 6). Correlation to the same lithostratigraphic interval at Hancheng section reveals much similarity in the number and relative thickness of magnetozones. Crucially there are two major normal polarity magnetozones (SCH4n and SCH5n) with a third tentative normal submagnetozone SCH5r.1n in this interval at SCH, likely to that in the GPTS and Buntsandstein Composite which also have three normal magnetozones. The wide sample spacing at Hancheng has probably missed the upper normal polarity magnetozone (SCH5r.1n) seen at SCH (Fig. 6). Overall, the relative thickness of magnetozones in the SCH3r–SCH5r is most similar to the Buntsandstein composite in the CG4r–CG7r interval. Thus, the IOB at SCH is placed at the base of SCH5n in the Lower part of the Liujiagou Formation (Fig. 6). However, a hiatus could be present given that there is an abrupt change in depositional environments from the shallow lacustrine facies of the Sunjiagou Formation to the overlying channelized, conglomeratic sandstones of the basal Liujiagou Formation. As a result, magnetozone SCH4n could be the equivalent of LT3n and SCH5n =LT4n. This would suggest that magnetochron LT2 is missing.

Like the underlying magnetozone interval SCH4r–SCH5, the succeeding thick normal SCH6n is more like the CG8n to CG10n interval in the Central German composite, than the marine-based magnetochrons LT5n to LT9n (Fig. 6), which range in age from the mid Smithian to late Spathian (Hounslow and Muttoni, 2010). Four reverse magnetozones within the LT5n–LT9n interval occur in arctic Canadian and Norwegian sections (Ogg and Steiner, 1991; Hounslow et al., 2008), but their thicknesses differ greatly compared to the equivalent interval in the Central German Composite. Notably, only two major reverse magnetozones (but 6 submagnetozones) were recovered from this interval at the Majiashan section (South China; Li et al., 2016; Fig. 6). At Majiashan, the cyclostratigraphically-calibrated polarity stratigraphy can be readily matched with the Central German Composite, providing important constraints for marine to non-marine correlations (Li et al., 2016; Fig. 6). No major reverse polarity magnetozones were detected within SCH6n, but three tentative submagnetozones SCH6n.1r–SCH6n.3r were detected (Fig. 4). However, in the nearby Hancheng section, reverse magnetozones O4r and O5r, straddling the Liujiagou and Heshanggou formations, were recognized (Ma et al., 1992; Fig. 6). The absence of such major reverse magnetozones at SCH could be related to local erosional loss. Sparse flora assigned to the *Pleuromeia sternbergii* assemblage in SCH6n interval suggests an Olenekian age (Wang and Wang, 1990), consistent with the magnetostratigraphic results. The Smithian–Spathian transition is marked by consistent normal polarity in arctic Canada, arctic Norway and South China, an interval which is likely condensed in the upper part of magnetochron LT6n due to a major boreal transgression (Ogg and Steiner, 1991; Hounslow et al., 2008; Li et al., 2016). It is likely that the well-defined reverse magnetozones O4r and O5r in Hancheng are equivalent to magnetozones MJ1r and MJ2r at Majiashan and LT6r–LT8r, CG8r–CG9n.2r in the reference sections (marked with blue correlated interval in Fig. 6). Hence the base of the Spathian is interpreted to be in the middle of SCH6n, in the uppermost of the Liujiagou Formation at SCH (Fig. 6).

Magnetozone SCH6r represents the late Spathian magnetochron LT9r and CG10r from the Buntsandstein (Fig. 6). This late Spathian reverse magnetochron has been widely recognized and contains at least one normal submagnetochron (Hounslow and Muttoni, 2010). Only normal polarity is found in the overlying Ermaying Formation (SCH7n or upper part of O6n) and is likely correlative to MT3n of the early Anisian (Fig. 6). The formational boundary is represented by a distinct sedimentary facies switch: the conglomeratic fluvial sandstones of the basal Ermaying Formation resting with erosional contact on the underlying red lacustrine siltstone-dominated Heshanggou Formation (Supplementary Fig. S1). The absence of the equivalent of magnetozone SCH6r in Hancheng was likely due to complete removal of the upper most Spathian LT9r. The brief magnetochrons MT1–2 of the GPTS, which characterize the Olenekian–Anisian transition, appear to be missing in many Chinese sections, and in other continental successions (Hounslow and Muttoni, 2010). The occurrence of the *Sinokannemeyeria* fauna and a CA-ID-TIMS U-Pb age (243.528±0.069 Ma), unequivocally place the Ermaying Formation within the Middle Triassic (Liu et al., 2018). Moreover, a diverse spinicaudatan *Protimonocarina-Euestheria* assemblage found in the lowermost part of the Ermaying Formation indicates an early Middle Triassic age (Wu, 1991). Accordingly, the base of the Anisian is placed within the hiatus between the Heshanggou and Ermaying formations, with magnetochons MT1 and MT2 being removed at the hiatus.

5.3 Magnetostratigraphic implications for the timing of the end-Permian terrestrial crisis in North China

The Permian–Triassic GSSP section at Meishan is thought to record two pulses of marine biotic extinctions (Song et al., 2013) at 251.941±0.037 Ma and 251.880±0.031 Ma (Burgess et al., 2014), all within the lower part of LT1n and its equivalents (Zhang et al., 2021; Fig. 7). At Shangsi, the distinctive changeover of conodonts from *Clarkina*-dominated to *Hindeodus*-dominated faunas (FO of *Hindeodus changxingensis*) marks the extinction interval, starting in bed 28a, within the lower part of magnetochron LT1n (Glen et al., 2007; Yuan et al., 2019; Fig. 7).

The timing of the terrestrial ecological crisis has been constrained by absolute ages or high-resolution chemostratigraphy (Fielding et al., 2019, 2021; Chu et al., 2020; Gastaldo et al., 2020).

Detailed sedimentological investigations in the Sydney Basin (eastern Australia), have demonstrated that the Permian–Triassic transitional sequences are stratigraphically complete, recording the disappearance of the *Glossopteris* flora within the top of the Bulli Coal (Fielding et al., 2019, 2021). The floral turnover occurred ~160–600 kyrs before the marine biotic crisis, according to several ID-TIMS ages from the basal Bulli Coal and basal Coalcliff Sandstone (Fielding et al., 2019, 2021). However, the relationship between the extinction interval and magnetic polarity cannot be precisely confirmed owing to the sampling gap in the coal bed (Fig. 7). In North China, collapse of terrestrial palaeofloras was marked by the extinction of approximately 54% of plant genera within the Sunjiagou Formation (Chu et al. 2019). This floral extinction slightly predated the latest Permian negative carbon-isotope excursion (Wu et al., 2020), and falls in magnetozone SCH2r (equivalent to magnetochron LP3r, immediately below LT1n; Fig. 7). According to our proposed magnetostratigraphic correlations, corroborated by our new absolute age (252.21±0.15 Ma), collapse of plant communities occurred about 270±150 kyrs earlier than the marine extinction (Fig. 7). Hence, our new magnetostratigraphic framework provides additional independent evidence that the terrestrial ecological crisis started before the marine mass extinction.

6 Conclusion

A detailed magnetostratigraphic investigation, spanning the early Changhsingian to early Anisian, was undertaken at the continental Shichuanhe section, yielding the first detailed Early Triassic non-marine timescale in North China. Results from the ~300 m thick red-bed dominated sequence exhibit dual polarity magnetizations, with the magnetic remanence mainly carried by hematite. The antipodal distributed directions are statistically undistinguishable to those expected in the Early

Triassic (Yang et al., 1991), pass the reversal test, and indicate a paleolatitude for the Shichuanhe section of 18.1°N.

Seven main magnetozones are recognized and the relative thickness of magnetozones displays good similarity, particularly to the composite from the Buntsandstein (Fig. 6). A new Late Permian CA-ID-TIMS U-Pb age of 252.21±0.15 Ma, provides direct evidence for the correlation of magnetozone SCH3n at Shichuanhe to magnetochron LT1n of the GPTS. According to our multi-disciplinary approach, the PTB is placed at ca. 8 m above the base of SCH3n, around the minimum of a negative $\delta^{13}C_{org}$ excursion, within the middle part of the Sunjiagou Formation. The spinicaudatan fauna within SCH3n is identical to that found in Central Germany within magnetozones CG3n–CG4n (equivalent to LT1n), adding additional paleontological support for our correlations. According to our composite magnetostratigraphy, base of the Olenekian is placed in the lower part of the Liujiagou Formation (base of SCH5n) and the Smithian–Spathian boundary in the upper part of the Liujiagou Formation. Combined magnetic polarity and sedimentary facies analysis reveal that the Spathian–Anisian transitional strata are absent.

With respect to the polarity timescale, destabilization of the terrestrial ecosystem in North China during the Permian–Triassic transition started within the upper part of magnetochron LP3r, 270±150 kyrs before the onset of the marine crisis, which falls within the base of the overlying normal magnetochron LT1n. The Shichuanhe section has preserves a complete terrestrial Permian–Triassic boundary record and is an important reference section for terrestrial and marine stratigraphic correlation.

Acknowledgements

We thank Yingchao Xu and Yiming Ma for the help in paleomagnetic data analysis. We also thank Haijun Song, Wenchao Shu, Kaixuan Ji, Yuyang Wu and Gan Liu for the invaluable advice in stratigraphic correlation and discussions about the PTME on land. This work was supported by the National Natural Science Foundation of China [grant number 41530104, 41661134047, 42030513], and the UK Natural Environment Research Council's Eco-PT Project (NE/P0137724/1), which is part of the Biosphere Evolution, Transitions and Resilience (BETR) Program.

Supplementary material

Supplementary file A, B, C

References

References

Benton, M.J., 2018. Hyperthermal-driven mass extinctions: killing models during the Permian–Triassic mass extinction. Philosophical Transactions of the Royal Society A: Mathematical, Physical and Engineering Sciences 376, 20170076. https://doi.org/10.1098/rsta.2017.0076.

Burgess, S.D., Bowring, S., Shen, S.Z., 2014. High-precision timeline for Earth's most severe extinction. Proceedings of the National Academy of Sciences 111, 3316–3321. https://doi.org/10.1073/pnas.1317692111.

Burgess, S.D., Bowring, S.A., 2015. High-precision geochronology confirms voluminous magmatism before, during, and after Earth's most severe extinction. Science Advances 1, e1500470. DOI: 10.1126/sciadv.1500470.

Cao, Y., Song, H.Y., Algeo, T.J., Chu, D.L., Du, Y., Tian, L., Wang, Y.H., Tong, J.N., 2019. Intensified chemical weathering during the Permian–Triassic transition recorded in terrestrial and marine successions. Palaeogeography, Palaeoclimatology, Palaeoecology 519, 166–177. https://doi.org/10.1016/j.palaeo.2018.06.012.

Chu, D.L., Tong, J.N., Benton, M.J., Yu, J.X., Huang, Y.F., 2019. Mixed continental-marine biotas following the Permian–Triassic mass extinction in South and North China. Palaeogeography, Palaeoclimatology, Palaeoecology 519, 95–107. https://doi.org/10.1016/j.palaeo.2017.10.028.

Chu, D.L., Grasby, S.E., Song, H.J., Dal Corso, J., Wang, Y., Mather, T.A., Wu, Y.Y., Song, H.Y., Shu, W.C., Tong, J.N., Wignall, P.B., 2020. Ecological disturbance in tropical peatlands prior to marine Permian–Triassic mass extinction: Geology 48, 288–292, https://doi .org/10.1130/G46631.1.

Chu, D.L., Dal Corso, J., Shu, W.C., Song, H.J., Wignall, P.B., Grasby, S.E., van de Schootbrugge, B., Zong, K.Q., Wu, Y.Y., Tong, J.N., 2021. Metal-induced stress in survivor plants following the end-Permian collapse of land ecosystems. Geology. https://doi.org/10.1130/G48333.1.

Davydov, V.I., Karasev, E.V., Nurgalieva, N.G., Schmitz, M.D., Budnikov, I.V., Biakov, A.S., Kuzina, D.M., Silantiev, V.V., Urazaeva, M.N., Zharinova, V.V., Zorina, S.O., Gareev, B., Vasilenko, D.V., 2021. Climate and biotic evolution during the Permian–Triassic transition in the temperate Northern Hemisphere, Kuznetsk Basin, Siberia, Russia. Palaeogeography, Palaeoclimatology, Palaeoecology, 110432. https://doi.org/10.1016/j.palaeo.2021.110432.

Fan, J.X., Shen, S.Z., Erwin, D.H., Sadler, P.M., MacLeod, N., Cheng, Q.M., Hou, X.D., Yang, J., Wang, X.D., Wang, Y., Zhang, H., Chen, X., Li, G.X., Zhang, Y.C., Shi, Y.K., Yuan, D.X., Chen, Q., Zhang, L.N., Li, C., Zhao, Y.Y., 2020. A high-resolution summary of Cambrian to Early Triassic marine invertebrate biodiversity. Science 367, 272–277. DOI: 10.1126/science.aax4953.

Feng, Z., Wei, H.B., Guo, Y., He, X.Y., Sui, Q., Zhou, Y., Liu, H.Y., Gou, X.D., Lv, Y., 2020. From rainforest to herbland: New insights into land plant responses to the end-Permian mass extinction. Earth-Science Reviews, 103153. https://doi.org/10.1016/j.earscirev.2020.103153.

Fetisova, A.M., Veselovskii, R.V., Latyshev, A.V., Rad’ko, V.A., Pavlov, V.E., 2014. Magnetic stratigraphy of the Permian–Triassic traps in the Kotui River valley (Siberian Platform): New paleomagnetic data. Stratigraphy and Geological Correlation 22, 377–390. https://doi.org/10.1134/S0869593814040054.

Fielding, C.R., Frank, T.D., McLoughlin, S., Vajda, V., Mays, C., Tevyaw, A.P., Winguth, A., Winguth, C., Nicoll, R.S., Bocking, M., Crowley, J.L., 2019. Age and pattern of the southern high-latitude continental end-Permian extinction constrained by multiproxy analysis. Nature Communications 10, 385, https://doi .org/10.1038/s41467-018-07934-z.

Gallet, Y., Krystyn, L., Besse, J., Saidi, A., Ricou, L.E., 2000. New constraints on the Upper Permian and Lower Triassic geomagnetic polarity timescale from the Abadeh section (central Iran). Journal of Geophysical Research: Solid Earth 105, 2805–2815. https://doi.org/10.1029/1999JB900218.

Gastaldo, R.A., Kamo, S.L., Neveling, J., Geissman, J.W., Bamford, M., Looy, C.V., 2015. Is the vertebrate-defined Permian–Triassic boundary in the Karoo Basin, South Africa, the terrestrial expression of the end-Permian marine event? Geology 43, 939–942.

Gastaldo, R.A., Neveling, J., Geissman, J.W., Kamo, S.L., 2018. A lithostratigraphic and magnetostratigraphic framework in a geochronologic context for a purported Permian–Triassic boundary section at Old (West) Lootsberg Pass, Karoo Basin, South Africa. Geological Society of America Bulletin 130, 1411–1438. https://doi.org/10.1130/B31881.1.

Gastaldo, R.A., Neveling, J., Geissman, J.W., Looy, C.V., 2019. Testing the *Daptocephalus* and *Lystraosaurus* assemblage zones in a lithostratographic, magnetostratigraphic, and palunological framework in the Free state, South Africa. Palaios 34, 542–561. https://doi.org/10.2110/palo.2019.019.

Gastaldo, R.A., Kamo, S.L., Neveling, J., Geissman, J.W., Looy, C.V., Martini, A.M., 2020. The base of the *Lystrosaurus* Assemblage Zone, Karoo Basin, predates the end-Permian marine extinction. Nature Communications 11, 1428. https://doi.org/10.1038/s41467-020-15243-7.

Grădinaru. E., Orchard, M.J., Nicora, A., Gallet, Y., Besse, J., Krystyn, L., Sobolev, E.S., Atudorei, N., Ivanova, D., 2007. The global boundary stratotype section and point (GSSP) for the base

of the Anisian stage: Deşli Caira Hill, North Dobrogea, Romania. Albertiana 36, 54–71.
Guo, W.W., Tong, J.N., Tian, L., Chu, D.L., Bottjer, D.J., Shu, W.C., Ji, K.X., 2019. Secular variations of ichnofossils from the terrestrial Late Permian–Middle Triassic succession at the Shichuanhe section in Shaanxi Province, North China. Global and Planetary Change 181, 102978. https://doi.org/10.1016/j.gloplacha.2019.102978.
Hounslow, M.W., 2006. PMagTools version 4.2-a tool for analysis of 2D and 3D directional data. http://dx.doi.org/10.13140/RG.2.2.19872.58880.
Hounslow, M.W., Balabanov, Y.P., 2018. A geomagnetic polarity timescale for the Permian, calibrated to stage boundaries. Geological Society, London, Special Publications 450, 61−103.
Hounslow, M.W., Muttoni, G., 2010. The geomagnetic polarity timescale for the Triassic: linkage to stage boundary definitions, in: Lucas, S.G. (Ed.), Triassic Timescale, 61–102.
Hounslow, M.W., Peters, C., Mork, A., Weitschat, W., Vigran, J.O., 2008. Biomagnetostratigraphy of the Vikinghogda Formation, Svalbard (Arctic Norway), and the geomagnetic polarity timescale for the Lower Triassic. Geological Society of America Bulletin 120, 1305–1325. https://doi.org/10.1130/B26103.1.
Huang, B.C., Yan, Y.G., Piper, J.D.A., Zhang, D.H., Yi, Z.Y., Yu, S., Zhou, T.H., 2018. Paleomagnetic constraints on the paleogeography of the East Asian blocks during Late Paleozoic and Early Mesozoic times. Earth-Science Reviews 186, 8–36. https://doi.org/10.1016/j.earscirev.2018.02.004.
IGCACS (Institute of Geology Chinese Academy of Geological Sciences), 1980. Mesozoic stratigraphy and paleontology of Shanganning Basin (I). Geological Publishing House, Beijing, pp. 1–212 [in Chinese].

Jaffey, A.H., Flynn, K.F., Glendenin, L.E., Bentley, W.C., Essling, A.M., 1971. Precision measurement of half-lives and specific activities of ^{235}U and ^{238}U. Physical review C 4, 1889–1906. DOI: https://doi.org/10.1103/PhysRevC.4.1889.

Ji, K.X., Wignall, P.B., Peakall, J., Tong, J.N., Chu, D.L., Pruss, S.B., 2021. Unusual intraclast conglomerates in a stormy, hot-house lake: The Early Triassic North China Basin. Sedimentology. doi: 10.1111/sed.12903.

Kamo, S.L., Czamanske, G.K., Krogh, T.E., 1996. A minimum U-Pb age for Siberian flood-basalt volcanism. Geochimica et Cosmochimica Acta 60, 3505–3511. https://doi.org/10.1016/0016-7037(96)00173-1.

Korte, C., Kozur, H.W., 2010. Carbon-isotope stratigraphy across the Permian–Triassic boundary: A review. Journal of Asian Earth Sciences 39, 215–235. https://doi.org/10.1016/j.jseaes.2010.01.005.

Kürschner, W.M., Herngreen, G.W., 2010. Triassic palynology of central and northwestern Europe: a review of palynofloral diversity patterns and biostratigraphic subdivisions. Geological Society, London, Special Publications 334, 263–283. https://doi.org/10.1144/SP334.11.

Lehrmann, D.J., Ramezani, J., Bowring, S.A., Martin, M.W., Montgomery, P., Enos, P., Payne, J.L., Orchard, M.J., Hongmei, W., Jiayong, W., 2006. Timing of recovery from the end-Permian extinction: Geochronologic and biostratigraphic constraints from south China. Geology 34, 1053–1056. https://doi.org/10.1130/G22827A.1.

Li, M.S., Ogg, J., Zhang, Y., Huang, C.J., Hinnov, L., Chen, Z.Q., Zou, Z.Y., 2016. Astronomical tuning of the end-Permian extinction and the Early Triassic Epoch of South China and Germany. Earth and Planetary Science Letters 441, 10–25. https://doi.org/10.1016/j.epsl.2016.02.017.

Liu, J., Ramezani, J., Li, L., Shang, Q., Xu, G., Wang, Y., Yang, J., 2018. High-precision temporal calibration of Middle Triassic vertebrate biostratigraphy: U-Pb zircon constraints for the *Sinokannemeyeria* Fauna and *Yonghesuchus*. Vertebrata PalAsiatica 55, 1–9. https://doi.org/10.19615/j.cnki.1000-3118.170808.

Liu, X.C., Wang, W., Shen, S.Z., Gorgij, M.N., Ye, F.C., Zhang, Y.C., Furuyama, S., Kano, A., Chen, X.Z., 2013. Late Guadalupian to Lopingian (Permian) carbon and strontium isotopic chemostratigraphy in the Abadeh section, central Iran. Gondwana Research 24, 222–232. https://doi.org/10.1016/j.gr.2012.10.012.

Lu, J., Zhang, P., Yang, M., Shao, L., Hilton, J., 2020. Continental records of organic carbon isotopic composition ($\delta^{13}C_{org}$), weathering, paleoclimate and wildfire linked to the End-Permian Mass Extinction. Chemical Geology 558, 119764. https://doi.org/10.1016/j.chemgeo.2020.119764.

Lurcock, P.C., Wilson, G.S., 2012. PuffinPlot: A versatile, user-friendly program for paleomagnetic analysis. Geochemistry, Geophysics, Geosystems 13, Q06Z45, doi:10.1029/2012GC004098.

Ma, X.H., Xing, L.S., Yang, Z.Y., Xu, S.J., Zhang, J.X., 1992. Paleomagnetic study since late Paleozoic in the Ordos basin, Seismological Press, Beijing, pp. 1–99 [in Chinese].

Meng, Q.R., Wu, G.L., Fan, L.G., Wei, H.H., 2019. Tectonic evolution of early Mesozoic sedimentary basins in the North China block. Earth-science reviews 190, 416–438. https://doi.org/10.1016/j.earscirev.2018.12.003.

McFadden, P.L., McElhinny, M.W., 1988. The combined analysis of remagnetization circles and direct observations in palaeomagnetism. Earth and Planetary Science Letters 87, 161–172. https://doi.org/10.1016/0012-821X(88)90072-6.

McFadden, P.L., McElhinny, M.W., 1990. Classification of the reversal test in palaeomagnetism.

Geophysical Journal International 103, 725–729. https://doi.org/10.1111/j.1365-246X.1990.tb05683.x.

Ogg, J.G., Steiner, M.B., 1991. Early Triassic magnetic polarity time scale-integration of magnetostratigraphy, ammonite zonation and sequence stratigraphy from stratotype sections (Canadian Arctic Archipelago). Earth and Planetary Science Letters 107, 69–89. https://doi.org/10.1016/0012-821X(91)90044-I.

Ouyang, S., Zhang, Z., 1982. Early Triassic palynological assemblage in Dengfeng, northwestern Henan. Acta Palaeontol. Sin. 21, 685–696 [in Chinese with English abstract].

Payne, J.L., Turchyn, A.V., Paytan, A., DePaolo, D.J., Lehrmann, D.J., Yu, M., Wei, J., 2010. Calcium isotope constraints on the end-Permian mass extinction. Proceedings of the National Academy of Sciences 107, 8543–8548. https://doi.org/10.1073/pnas.0914065107.

Ramezani, J., Hoke, G.D., Fastovsky, D.E., Bowring, A.S., Therrien, F., Dworkin, S.I., Atchley, S.C., Nordt, L.C., 2011. High-precision U-Pb zircon geochronology of the Late Triassic Chinle Formation, Petrified Forest National Park (Arizona, USA): Temporal constraints on the early evolution of dinosaurs. GSA Bulletin 123: 2142–2159. https://doi.org/10.1130/B30433.1.

Scholze, F., Wang, X., Kirscher, U., Kraft, J., Schneider, J.W., Götz, A.E., Joachimski, M.M., Bachtadse, V., 2017. A multistratigraphic approach to pinpoint the Permian–Triassic boundary in continental deposits: The Zechstein–Lower Buntsandstein transition in Germany. Global and Planetary Change 152, 129–151. https://doi.org/10.1016/j.gloplacha.2017.03.004.

Shen, S.Z., Crowley, J.L., Wang, Y., Bowring, S.A., Erwin, D.H., Sadler, P.M., Cao, C.Q., Rothman, D.H., Henderson, C.M., Ramezani, J., 2011. Calibrating the end-Permian mass extinction. Science 334, 1367–1372. DOI: 10.1126/science.1213454.

Song, H., Wignall, P.B., Tong, J., Yin, H., 2013. Two pulses of extinction during the Permian–Triassic crisis. Nature Geoscience 6, 52–56. https://doi.org/10.1038/ngeo1649.

Song, H.J., Wignall, P.B., Dunhill, A.M., 2018. Decoupled taxonomic and ecological recoveries from the Permo–Triassic extinction. Sci Adv 4, eaat5091. DOI: 10.1126/sciadv.aat5091.

Steiner, M.B., 2006. The magnetic polarity time scale across the Permian–Triassic boundary. Geological Society, London, Special Publications 265, 15–38. https://doi.org/10.1144/GSL.SP.2006.265.01.02.

Sun, Y.D., Joachimski, M.M., Wignall, P.B., Yan, C.B., Chen, Y.L., Jiang, H.S., Wang, L.N., Lai, X.L., 2012. Lethally hot temperatures during the Early Triassic greenhouse. Science 338, 366–370. DOI: 10.1126/science.1224126.

Sun, Z.M., Hounslow, M.W., Pei, J.L., Zhao, L.S., Tong, J.N., Ogg, J.G., 2009. Magnetostratigraphy of the Lower Triassic beds from Chaohu (China) and its implications for the Induan–Olenekian stage boundary. Earth and Planetary Science Letters 279, 350–361. https://doi.org/10.1016/j.epsl.2009.01.009.

Szurlies, M., 2007. Latest Permian to Middle Triassic cyclo-magnetostratigraphy from the Central European Basin, Germany: Implications for the geomagnetic polarity timescale. Earth and Planetary Science Letters 261, 602–619. https://doi.org/10.1016/j.epsl.2007.07.018.

Szurlies, M., 2013. Late Permian (Zechstein) magnetostratigraphy in Western and Central Europe. Geological Society, London, Special Publications 376, 73–85. https://doi.org/10.1144/SP376.7.

Tong, J.N., Chu, D.L., Liang, L., Shu, W.C., Song, H.J., Song, T., Song, H.Y., Wu, Y.Y., 2019. Triassic integrative stratigraphy and timescale of China. Science China (Earth Sciences) 62, 189–222. https://doi.org/10.1007/s11430-018-9278-0.

Wang, Z.Q., Wang, L.X., 1982. A new species of the lycopsid *Pleuromeia jiaochengensis* from the Early Triassic of Shanxi, China and its ecology. Palaeontology 25, 215–226.

Wang, Z.Q., Wang, L.X., 1990. New plant assemblages from the bottom of the Mid-Triassic Ermaying Formation. Shanxi Geology 5, 303–318 [in Chinese with English abstract].

Ward, P.D., Botha, J., Buick, R., De Kock, M.O., Erwin, D.H., Garrison, G.H., Kirschvink, J.L., Smith, R., 2005. Abrupt and Gradual Extinction Among Late Permian Land Vertebrates in the Karoo Basin, South Africa. Science 307, 709–714. DOI: 10.1126/science.1107068.

Wignall, P.B., 2015, The Worst of Times: How Life on Earth Survived Eighty Million Years of Extinction: Princeton, New Jersey, Princeton University Press, pp. 1–224.

World Magnetic Model 2019–2024; https://www.ngdc.noaa.gov/geomag/calculators/magcalc.shtml#igrfwmm.

Wu, T.Y., 1991. Conchostracan assemblage from bottom of Ermaying Formation, Shaanxi. 30, 631–642. [in Chinese with English abstract].

Wu, Y.Y., Tong, J.N., Algeo, T.J., Chu, D.L., Cui, Y., Song, H.Y., Shu, W.C., Du, Y., 2020. Organic carbon isotopes in terrestrial Permian-Triassic boundary sections of North China: Implications for global carbon cycle perturbations. Geological Society of America Bulletin 132, 1106–1118. https://doi.org/10.1130/B35228.1.

Wu, Y.Y., Chu, D.L., Tong, J.N., Song, H.J., Dal Corso, J., Wignall, P.B., Song, H.Y., Du, Y., Cui, Y., 2021. Six-fold increase of atmospheric pCO2 during the Permian–Triassic mass extinction. Nature Communications 12, 2137. https://doi.org/10.1038/s41467-021-22298-7.

Yang, Z.Y., Ma, X.H., Besse, J., Courtillot, V., Xing, L.S., Xu, S.J., Zhang, J.X., 1991. Paleomagnetic results from Triassic sections in the Ordos Basin, North China. Earth and

Planetary Science Letters 104, 258–277. https://doi.org/10.1016/0012-821X(91)90208-Y.

Yin, H.F., Zhang, K.X., Tong, J.N., Yang, Z.Y., Wu, S.B., 2001. The global stratotype section and point (GSSP) of the Permian–Triassic boundary. Episodes 24, 102–114.

Yuan, D.X., Shen, S.Z., Henderson, C.M., Chen, J., Zhang, H., Zheng, Q.F., Wu, H.C., 2019. Integrative timescale for the Lopingian (Late Permian): A review and update from Shangsi, South China. Earth-Science Reviews 188, 190–209. https://doi.org/10.1016/j.earscirev.2018.11.002.

Zhang, M., Qin, H.F., He, K., Hou, Y.F., Zheng, Q.F., Deng, C.L., He, Y., Shen, S.Z., Zhu, R.X., Pan, Y.X., 2021. Magnetostratigraphy across the end-Permian mass extinction event from the Meishan sections, southeastern China. Geology. https://doi.org/10.1130/G49072.1.

Zhu, R.K., Xu, H.X., Deng, S.W., Guo, H.L., 2007. Lithofacies palaeogeography of the Permian in northern China. J. Palaeogeogr 9, 133–142 [in Chinese with English abstract].

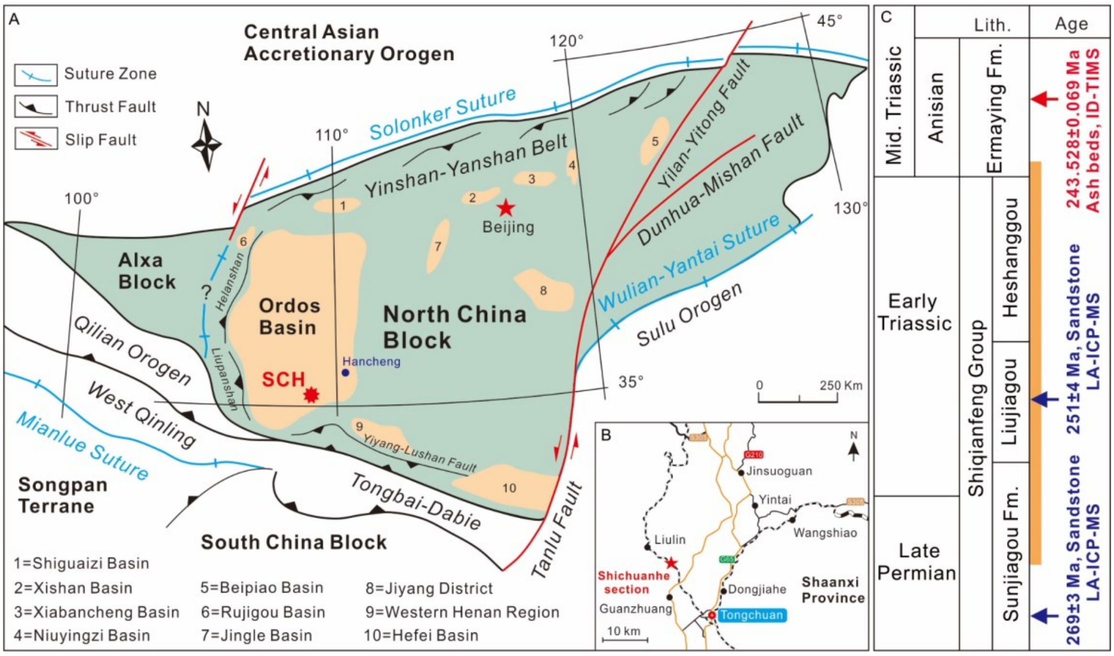

Fig 1. Simplified paleotectonic map of the North China Block and its sedimentary basins (modified from Meng et al., 2019). Red star marks the studied Shichuanhe (SCH) section. Blue point indicates the Hancheng section. Inset B shows a detailed location of the SCH section. C. Brief Permian–Triassic chrono- and lithostratigraphic framework in North China. ID-TIMS age is from Liu et al. (2018), LA-ICP-MS ages are from Zhu et al. (2019). Orange bar represents studied interval.

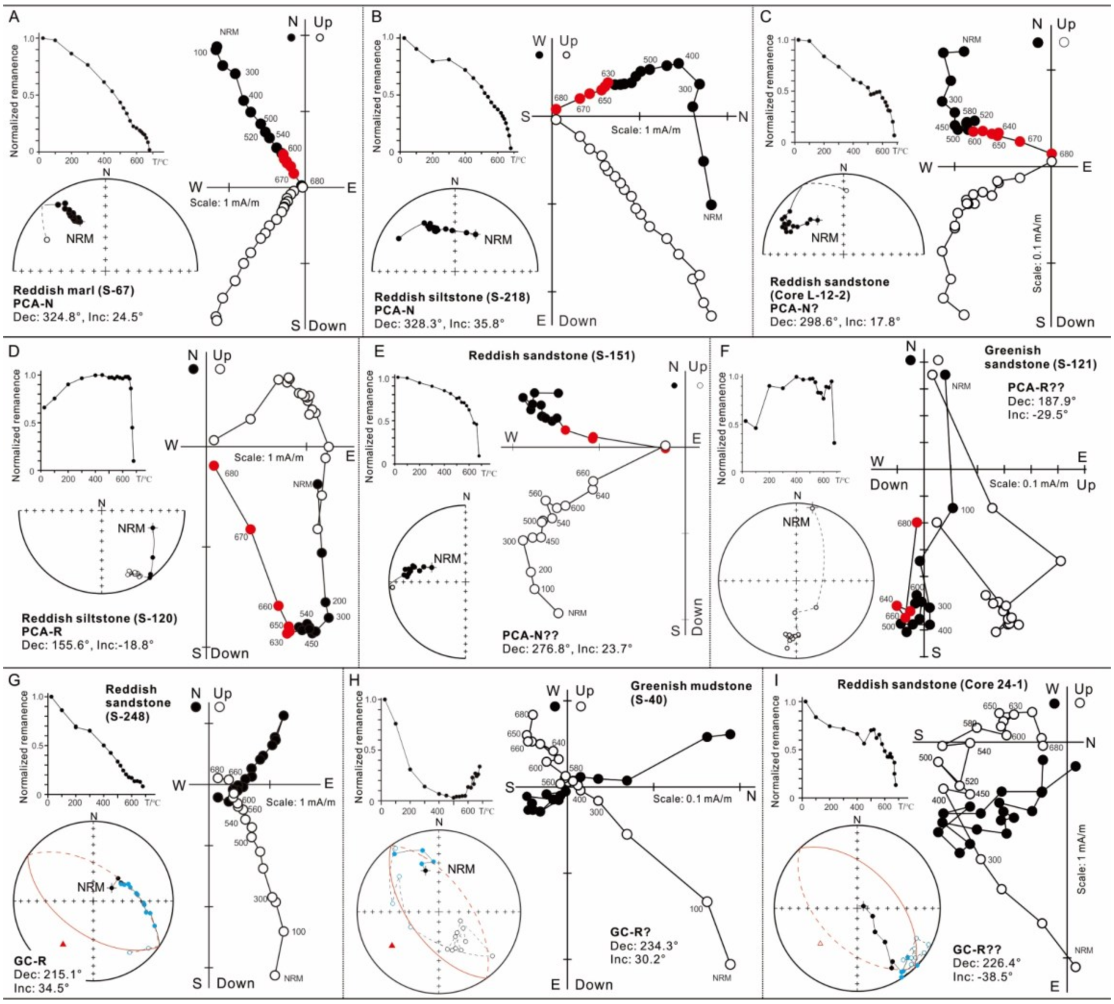

Fig 2. Representative demagnetization behaviors with polarity interpretation of specimens from Shichuanhe section. A–F: Principal Component Analysis (PCA), steps used for ChRM line-fits are highlighted in red. A. A largely single component magnetization shows a stable end-point that is close to expected Early Triassic direction in North China (polarity N; S1 class), Sunjiagou Formation. B. After removal of an eastward LTC below 400°C, specimen shows good linearity to the origin with the ChRM from 630–680°C steps, polarity N (S1), Heshanggou Formation. C. Similar demagnetization behavior to B, but the ChRM direction is a little deviated from expected direction (N?, S2), Liujiagou Formation. D. Two component magnetizations with the CHRM 630°C to the origin (R, S1). Apparent mid-stable component is from blocking temperature overlap between the ChRM and the LTC, Sunjiagou Formation. E. Specimen shows good linearity above 600°C, but isolated ChRM is deviated from expected direction (N??, S3), Liujiagou Formation. F. The last three steps show moderately linear ChRM component and the LTC is a composite LTC and Triassic reverse component (R??, S3), Sunjiagou Formation. Filled (open) symbols are lower (upper) hemisphere. G–I: Great-circle (GC) fits, red arc represents fitted great circle and blue indicates

points used. Lower projection paths dashed and upper projection paths are solid. G. Great circle plane from 200–680°C, specimen shows unscattered great circle trend towards the expected reverse direction (R, T1). LTC (100–500°C) is likely a composite component, Heshanggou Formation. H. Well-defined LTC 100–400 °C and a somewhat scattered trend (moderate arc length 100–540°C) towards Triassic reverse, with erratic directions above 600°C, due to thermal alteration (R?, T2), Sunjiagou Formation. I. Well-defined LTC NRM–400°C and a trend towards expected Triassic reverse direction with the great circle fitted to the higher temperature steps (R??, T3), Liujiagou Formation.

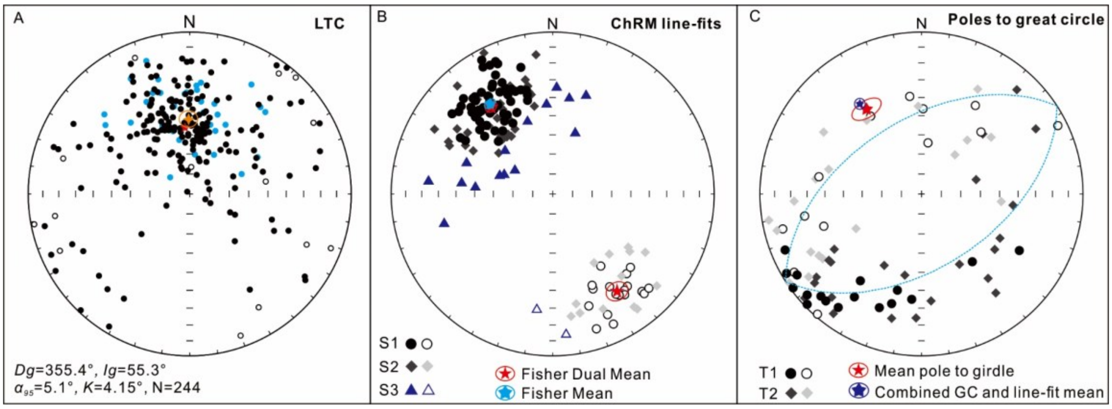

Fig 3. Equal-area stereographic projection of the low-temperature components (LTC) and characteristic (ChRM) components of the Shichuanhe section. A. LTC in geographic coordinates, with the Fisher means (red star) close to the recent geomagnetic dipole field direction (orange star) at the SCH site (IGRF, computed from https://www.ngdc.noaa.gov/geomag/calculators/magcalc.shtml#igrfwmm). B. Dual polarity ChRM line fits (in stratigraphic coordinates), with calculated Fisher (dual) mean (only S1 and S2 data used) and Fisher means of all converted to normal (Blue star with 95% confidence ellipse). C. Poles to the great circle planes of T1 and T2 class data, along with the mean of the combined great circle and line-fits (McFadden and McElhinny, 1988). The single girdle plane (dotted) is the plane normal to the mean direction calculated using both the great circle poles and ChRM fits. Red star indicates the mean pole to the great circle girdle of points and its elliptical 95% confidence cone. The filled (open) circles refer to the lower (upper) hemisphere, respectively.

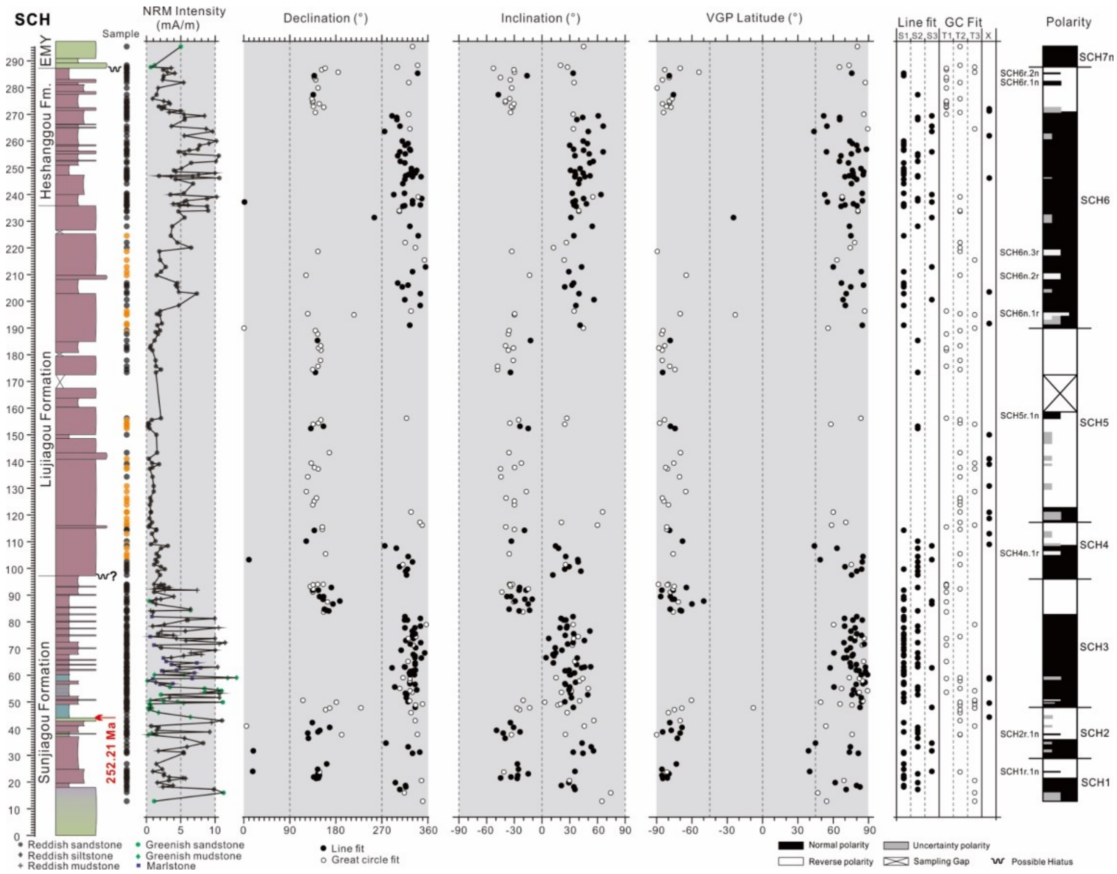

Fig 4. Magnetostratigraphy of the Shichuanhe (SCH) section with polarity quality ratings. Demagnetization behavior of S and T refer to ChRM line-fits (filled circles) and great circle fits (open circles), respectively, which are subdivided into S1, S2, S3 and T1, T2, T3 class (see text for details). Specimens with no Triassic magnetization are marked X. Half-width bars indicate a single sample with high quality (S1, S2 or T1, T2), showing opposite polarity interpretation with respect to adjacent samples. For the gray bar, one-quarter-width means single poorest quality or undetermined polarity (S3, T3 and X), whereas half-width indicates successive poorest or undetermined polarities.

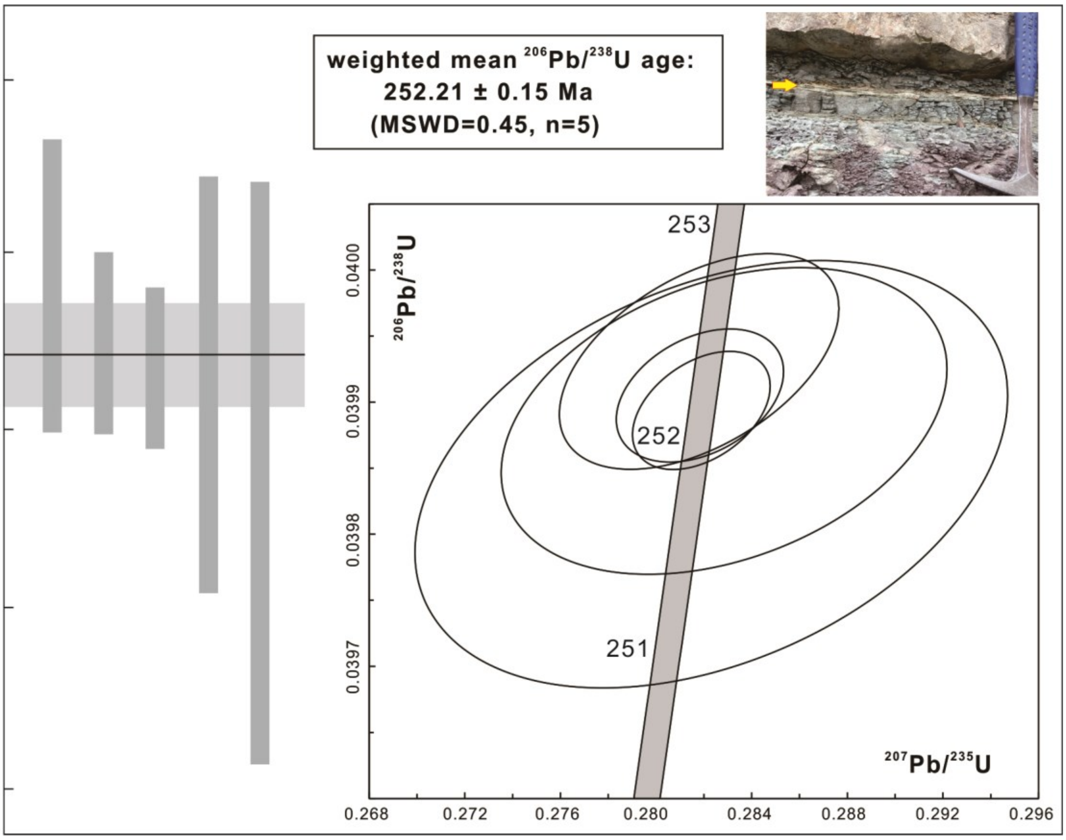

Fig 5. Concordia diagram and ranked $^{206}Pb/^{238}U$ plot analyzed zircon grains from the Shichuanhe ash bed (upper right inset marked by yellow arrow). Each vertical bar represents a single zircon analysis included in the weighted mean age and the bar height is proportional to the 2σ analytical uncertainty. The horizontal black line and grey bar represent the calculated weighted mean age and its 2σ analytical uncertainty envelope, respectively. Outliers excluded from age calculation plot outside the diagram area are not shown herein.

	Mean site direction (°)								Reversal test (G_o/G_c)	Virtual Geomagnetic Pole (VGP) (°)			
	Polarity	D_g	I_g	D_s	I_s	K_s	α_{95}	N		Lat.	Long.	δp/δm	Paleolat.
Shichuanhe section (Tongchuan)													
Line fit[$]	Normal	324.9	39.0	325.0	34.0	26.54	2.9	93					
	Reverse	145.1	-33.9	146.4	-28.5	28.31	4.9	31					
	All	324.9	37.7	325.4	32.6	26.54	2.5	124	Rb (5.67/5.74)*	54.7	358.6	1.60/2.84	17.7 N
GC fit[#]	All	328.6	44.2	327.3	37.0	16.36	4.2	73					
Combined[+]	Normal	325.5	39.6	325.6	34.1	24.14	2.7	118					
	Reverse	145.4	-37.2	145.7	-32.3	21.19	3.5	79					
	All	325.5	38.4	325.6	33.3	14.30	1.9	197	Ra (1.82/4.38)*	55.2	359.0	1.23/2.16	18.1 N
Hancheng (Yang et al., 1991)													
Line fit[$]	Normal	334.7	34.3	334.2	30.0	114.8	4.8	9 (sites)		61.2	349.5		
	Reverse	160.2	-32.5	156.4	-31.7	48.8	8.7	7 (sites)		62.1	345.2		
	All	337.1	33.5	335.2	32.5	76.7	4.2	16 (sites)	Rb (2.54/8.82)*	61.7	347.6		17.6 N
Tongchuan, LJG (Ma et al., 1992)													
Line fit[$]	All	330.1	43.2	329.7	32.4	165	6.0	5 (sites)		58.0	354.1	3.8/6.8	17.6 N

$: conventional Fisher mean. #: Great Circle mean. +: Combined line fit and great circle fit (McFadden and McFadden, 1988). D_g, I_g and D_s, I_s : declination and inclination in geographic and stratigraphic coordinates, respectively. K_s: precision parameter after tilt correction. α_{95}: half-angle of cone of 95% confidence about the mean direction in stratigraphic coordinate. N: number used to calculated the mean direction. Lat. and Long.: latitude and longitude of the mean virtual geomagnetic pole, respectively. δp/δm : semi-axes of the 95% confidence level ellipse on palaeomagnetic pole. Paleolat.: calculated paleolatitude.
Reversal test (McFadden and McElhinny, 1990). G_o is the angular separation between the inverted reserve and normal directions and G_c is the critical value for the reverse test. In the reversal test, G_o/G_c marked * suggest a common K value. R_a and R_b mean positive reversal test with critical angle that R_a<5° and R_b<10°.

Table 1. Permian–Triassic mean directions and virtual geomagnetic poles for the Shichuanhe section and other sections in North China. Paleolatitude and reversal test of Yang et al. (1991) were not provided in the original study.

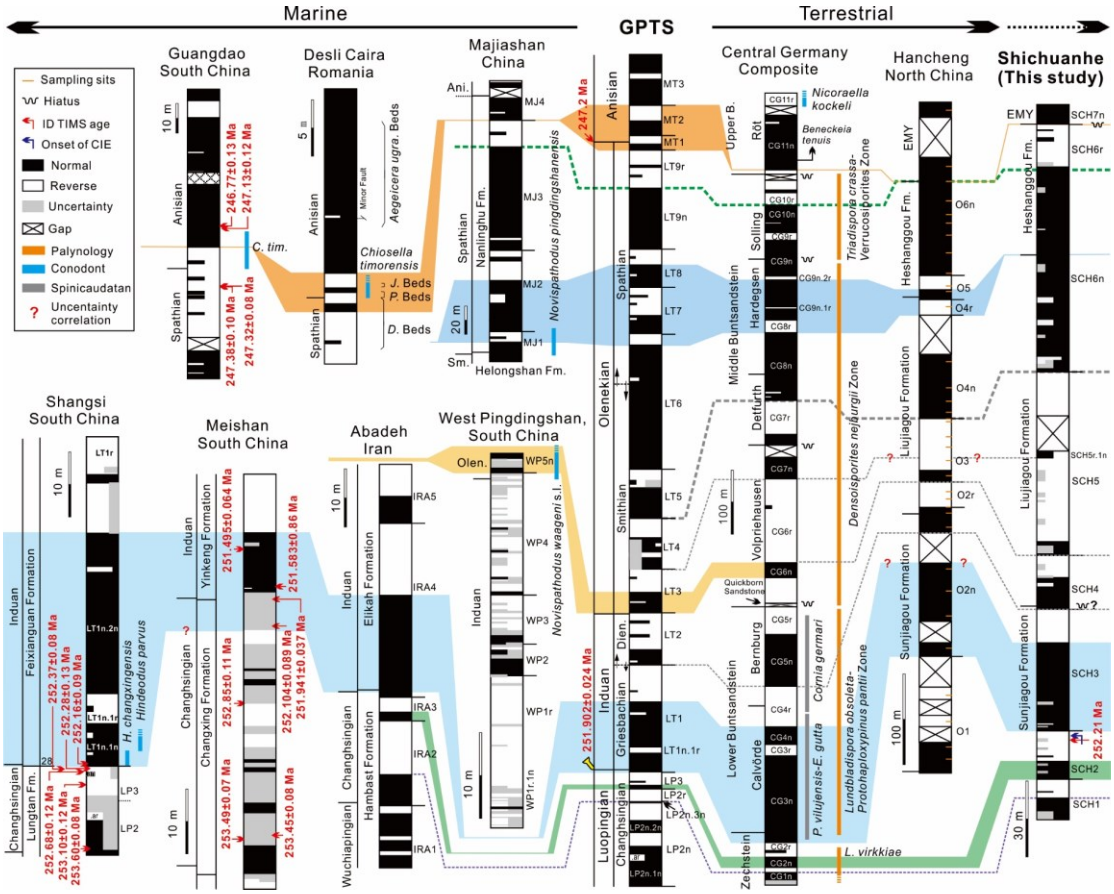

Fig 6. Changhsingian–Anisian magnetic polarity stratigraphy of North China and comparison with other non-marine and marine successions. Geomagnetic polarity timescale (GPTS) is based on Hounslow and Muttoni (2010) and Hounslow and Balabanov (2018). Compiled Central German Composite and biostratigraphy (Szurlies, 2007, 2013; Kürschner and Herngreen, 2010; Scholze et al., 2017). Hancheng section (Ma et al., 1992). Distance between sampling sites >30 m is marked by a sampling gap. West Pingdingshan (Sun et al., 2009), Majiangshan (Li et al., 2016), Meishan (Modified from Hounslow and Balabanov, 2018), Abadeh (Gallet et al., 2000; Szurlies, 2013), Guangdao (Lehrmann et al., 2006), Shangsi (Hounslow and Balabanov, 2018; Yuan et al., 2019). Desli Caira (Grădinaru et al., 2007). Question marks indicate uncertain correlations. *D.* Beds=*Deslicairites* Beds; *P.* Beds=*Paracrocordicera* Beds; *J.* Beds=*Japonites* Beds; *P. vilujensis–E. gutta*=*Palaeolimnadiopsis vilujensis–Euetheria gutta*; *L. virkkiae*=*Lueckisporites virkkiae* Zone.

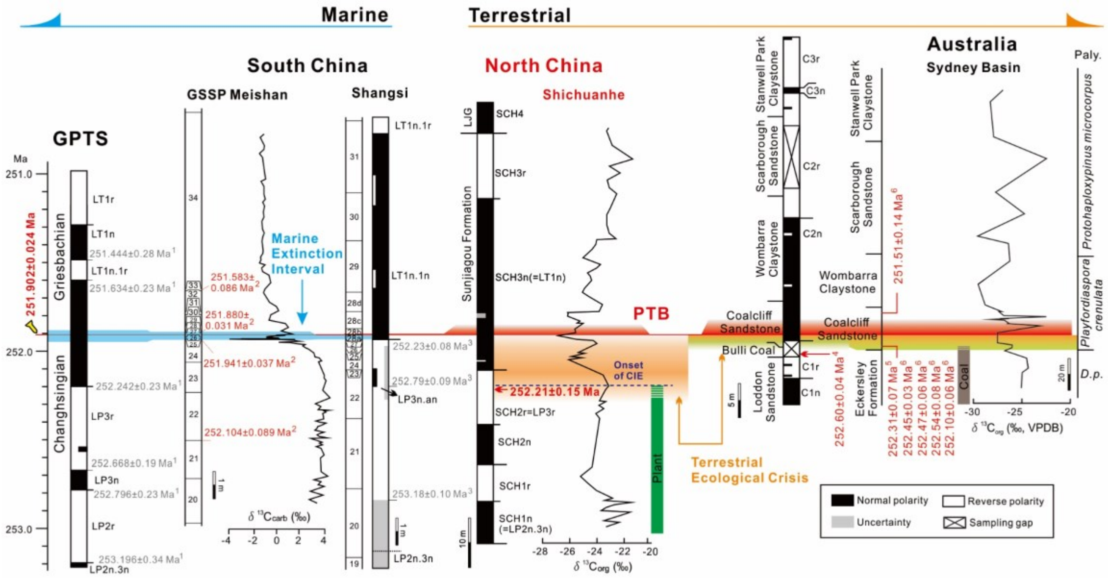

Fig 7. Correlation of the Permian–Triassic interval sequence at Shichuanhe with the GSSP at Meishan (Burgess et al., 2014), Shangsi (Yuan et al., 2019) and Australian sections (Belica, 2017; Fielding et al., 2019, 2021). Ages of [1]=calculated by Hounslow and Balabanov, 2018, [2]=Burgess et al., 2014, [3]=calculated magnetozone boundary ages by Yuan et al., 2019, [4]=Metcalfe et al., 2015, [5]=Fielding et al., 2019, [6]=Fielding et al., 2021. GPTS is from (Hounslow and Balabanov, 2018). Carbon isotope curve of Shichuanhe (Wu et al., 2020). Paly.=Palynostratigraphy (Mays et al., 2020). *D.p.=Dulhuntyispora parvithola* Zone.

Supplementary Data A

This Supplementary data contains the following sections.

1. Sedimentology of the continental Shichuanhe Section (SCH)

    Figure S1. Log of Shichuanhe section showing the lithology, sedimentary structures, depositional environments and the magnetic sampling positions

    Figure S2. Photographs of the formation boundaries and representative sedimentary features of the Shichuanhe section.

2. Additional rock magnetic information

    2.1 NRM intensity

    Figure S3. Variations of NRM intensity with lithology

    2.2 Thermomagnetic curve

    Figure S4. Magnetic susceptibility versus temperature (K-T) curves of typical specimens

3. U-Pb geochronology methods and results

    Figure S5. U-Pb dating results for zircons analyzed by LA-ICP-MS

4. Additional demagnetization data and palaeomagnetic mean directions

    Figure S6–S10. Demagnetization behavior and the interpreted polarity of different lithologies

    Table S1. Mean directions, reversal test and virtual geomagnetic poles for specimens with different quality-ratings.

5. Supplementary References

1. Sedimentology of the Shichuanhe Section (SCH)

Five facies associations (FAs) have been recognized at SCH, based on lithology, their stratigraphic packeting patterns, and physical sedimentary structures. More detailed sedimentological investigations in North China have been undertaken by Ji et al. (under review). Here we briefly represent the sedimentological feature throughout the SCH section (Fig. S2) and focus on the Permian–Triassic boundary sequence.

FA1 is characterized by multistorey fine– to medium– grained sandstone up to 2 m thick, interbedded with thin red mudstones. This facies marks the lowermost and topmost parts of the section with green colored sandstones. This facies also forms the main part of the Liujiagou Formation with typical red coloration (Fig. S1). Trough and tabular cross-beddings and parallel laminations are common, ripple marks and desiccation cracks are occasionally present, especially in the lower Liujiagou Formation. Sand bodies in the basal Liujiagou Formation display slightly undulating but sharp contacts (Fig. S2E). Lag conglomerates of mudstone intraclasts are quite common (Fig. S2F) and flute casts preserved on the soles of sandstone beds are also found. The sharply bounded sandstones are stacked into lenticular channelized beds (Fig. S2G).

FA2 consists of massive red mudstone, interbedded with thin rippled siltstones and paleosols are well-developed in this facies (including inceptisols succeeding aridisols), coupled with some root traces and burrows (Guo et al., 2019; Yu et al., 2022). This fine-grained facies is interpreted to be deposited under alluvial floodplain settings.

FA3 is represented by alternating red, fine-grained calcareous sandstone and silty mudstone, with some marlstone interlayers (Fig. S2C), with occasional desiccation cracks and calcretes . This facies association is interpreted as formed in coastal environments (Ji et al., under review). Typically, the lower parts of FA3 in the section are characterized by green and red alternating mudstone and thin interbedded marlstones, and sandstones (Fig. S2B). These contain mixed terrestrial spinicaudatans and marine bivalves, which were affected by northeastwards directed regional marine transgressions (Chu et al., 2019). The inferred PTB lies in the upper part of this distinct interval.

FA4 is distributed around the middle part of the Liujiagou formation, and is comprised of fine-grained sandstone and lenticular intraformational conglomerates, interleaved with dark red siltstone and mudstone. This facies association is formed in fluviodeltaic environments (Ji et al., under review).

FA5 is represented by rhythmic alternations of sandstone up to 20–50 cm thick and massive siltstone, with paleosols and trace fossils which are especially well developed in this interval (Yu et al., 2022). FA5 records an environment that was dominated by fine-grained deposition on alluvial plains, with frequent subaerial exposure.

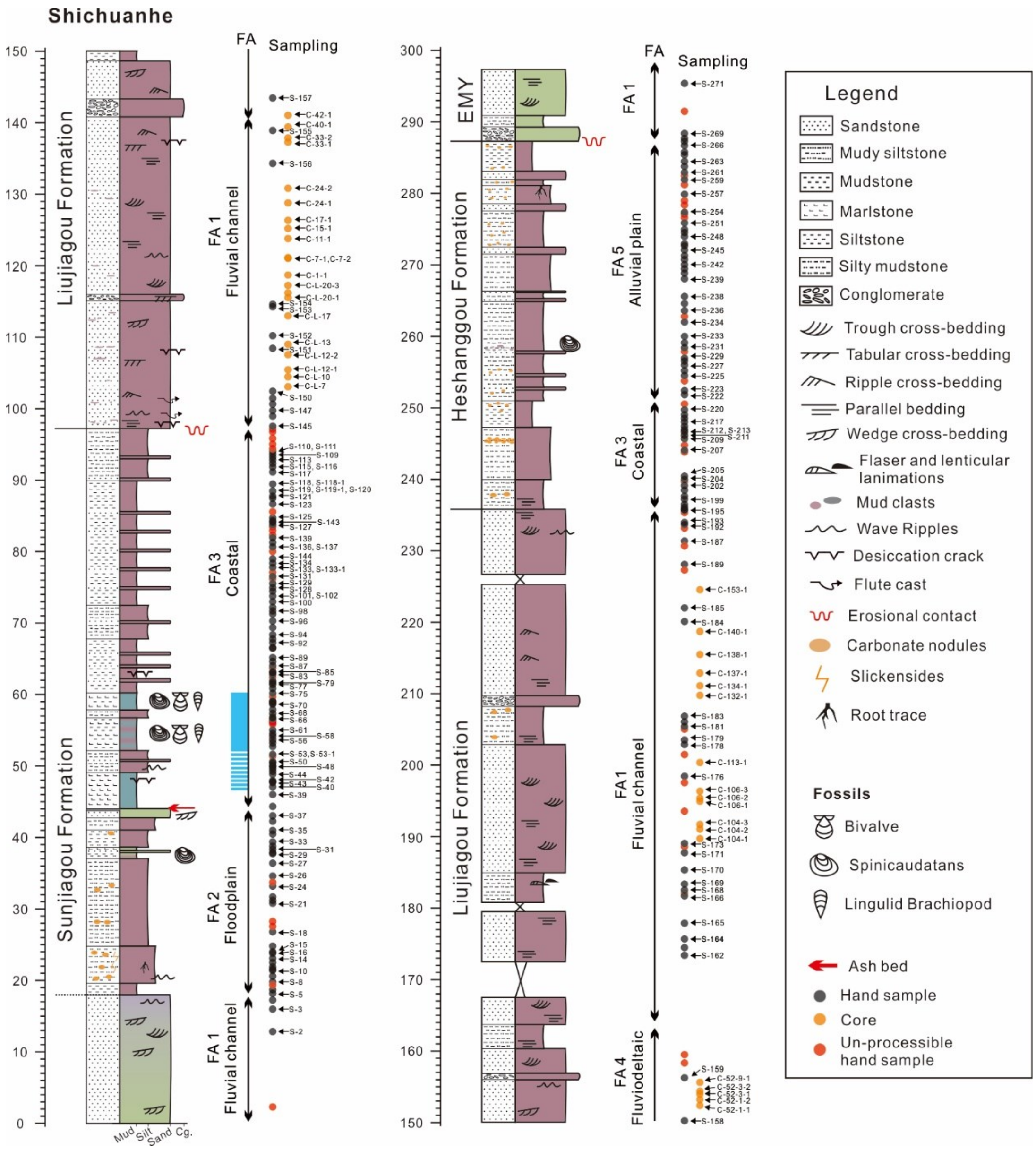

Figure S1. The Shichuanhe section showing lithology, sedimentary structures, depositional environments and the paleomagnetic sampling positions. Blue bar on the facies association represents an interval influenced by marine flooding .

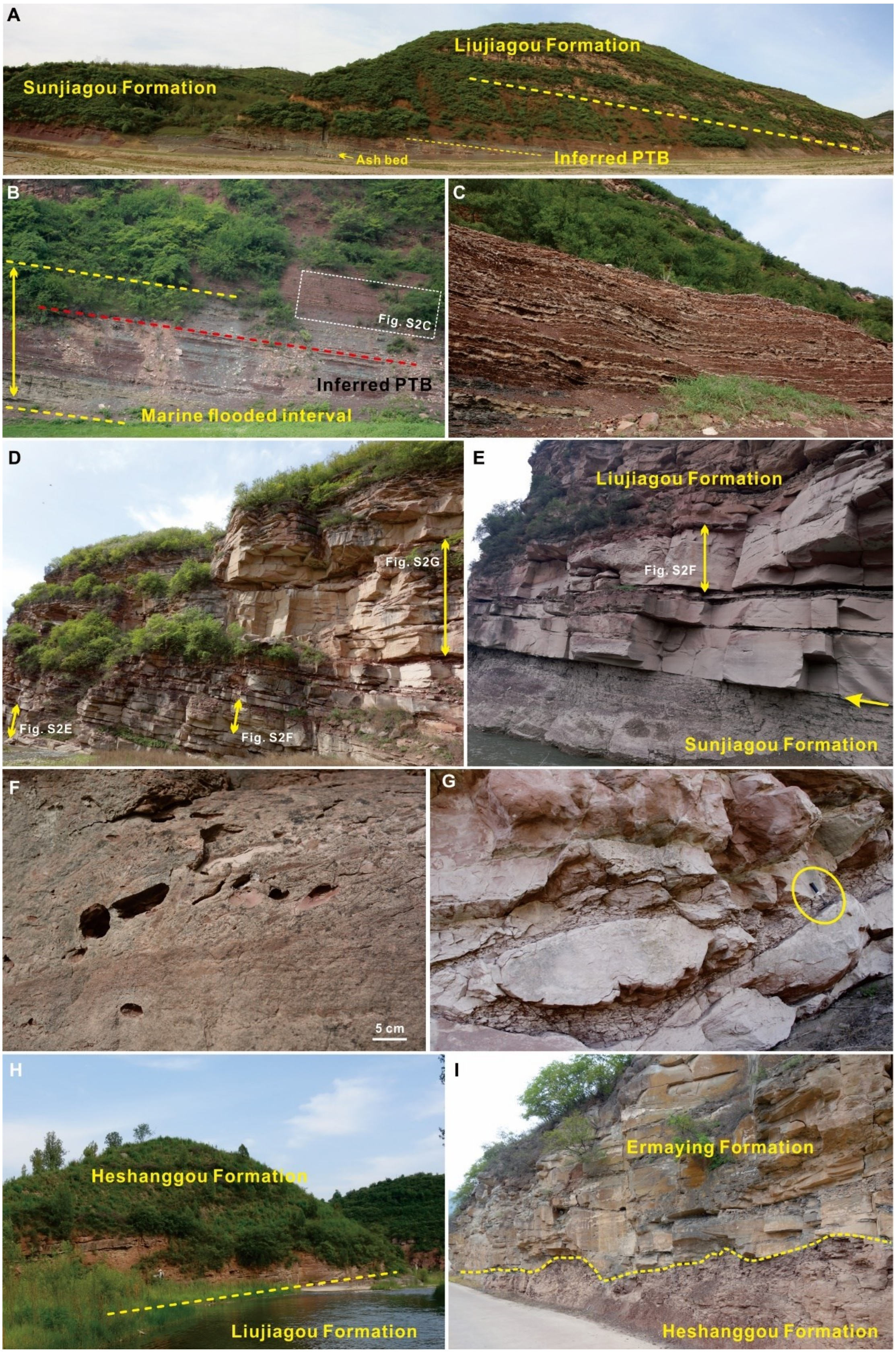

Figure S2. Formation boundaries and representative sedimentary features of the Shichuanhe section. A), Sunjiagou and the overlying Liujiagou formations with the inferred PTB and the radioisotopically-dated ash bed indicated. B), Marine flooding influenced interval in the middle part of the Sunjiagou Formation, which is characterized by green mudstone where the mixed marine-terrestrial biota was found (Chu et al., 2019). The inferred PTB lies close to the top of the photograph. C), Alternating mudstone and sandstone just above the PTB, as showed in inset in B. (D), Multistorey sandstones in the lower portion of the Liujiagou Formation. E), The lowermost massive fine-grained sandstone displays a low-relief erosional contact (at sharp contact) with the underlying mud-rich (coastal environment) of the upper Sunjiagou Formation. F), Mud clasts of a varied size are common and weathered out leaving the holes. G), The laterally extensive sand-bodies are stacked lenticular channellised sandstones. The hammer is 25 cm in length. H), Thick sandstone of the uppermost Liujiagou Formation fining-upwards to the overlying red siltstone-dominated Heshanggou Formation, with a conformable contact. I), Green massive sandstones of the basal Ermaying Formation overlying the Heshanggou Formation, with a clear erosional contact (dotted line).

2. Magnetic information

2.1 NRM intensity

At the Shichuanhe section several lithologies were encountered. Green sandstone present in the lowermost and topmost parts of the section. The Permian–Triassic Boundary interval is dominated by red siliciclastics, with green mudstone occurring in the middle part of the Sunjiagou Formation within the marine influenced interval. Marlstone intervals are scattered in the upper of the Sunjiagou Formation. Generally, reddish sediments have higher (untreated) natural remanent magnetization (NRM) intensities than the greenish lithologies (Fig. S3). Around half of the mudstones have rather lower NRM intensities < 1 mA/m, although exceptions up to 30 mA/m occur. Generallyred siltstone and mudstone have higher NRM intensity than reddish sandstone. The sandstone dominated Liujiagou Formation has the lowest NRM intensity with respect to the Sunjiagou and Heshanggou formations.

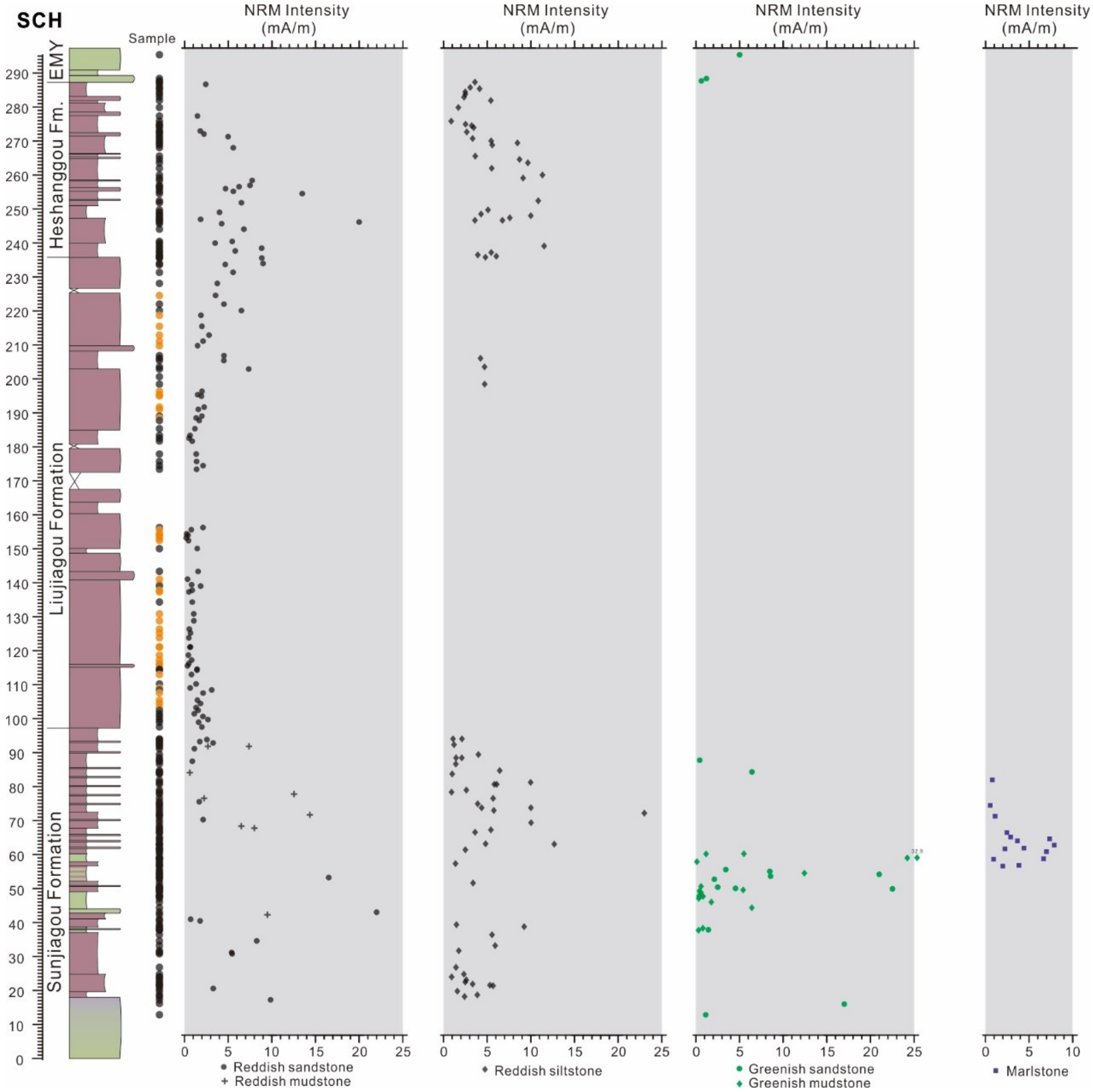

Figure S3. Variations of NRM intensity with lithology and body color. You need a mA/m scale on all these plots

2.2 Thermomagnetic curve

The temperature dependence of magnetic susceptibility during heating and cooling cycles of typical samples were measured in air (Fig. S4). All specimens display low initial susceptibility which mostly decreases with increasing temperature. The heating and cooling curves are largely irreversible, with cooling curves show conspicuously higher susceptibilities below 585℃, which probably indicates newly formed magnetite due to clay and/or Fe-silicate decomposition during heating (Deng et al., 2001; Jiang et al., 2015). For the green lithologies (specimens S-40 and S-54), distinct drops in susceptibility are observed at 500-580℃, corresponding to the Curie temperature of magnetite. The subsequent small rise of magnetic susceptibilities above 600℃ could be uncorrected drift or additional oxidation/alteration. For the red sediment samples the susceptibilities consistently decrease to 700℃, indicative of hematite. Specimen S-216 shows a clear rise of susceptibility from 450℃, which then decreases in the vicinity of 585℃ and near 700℃, implying the presence of both magnetite and hematite (although the magnetite may be alteration-generated from heating starting at ca. 450ºC). Goethite is probably also present according to the drop of susceptibility upon heating below 100℃ (De Boer and Dekkers, 1998). Thus, the main magnetic carriers at SCH are mainly hematite, with magnetite more important in the greener lithologies.

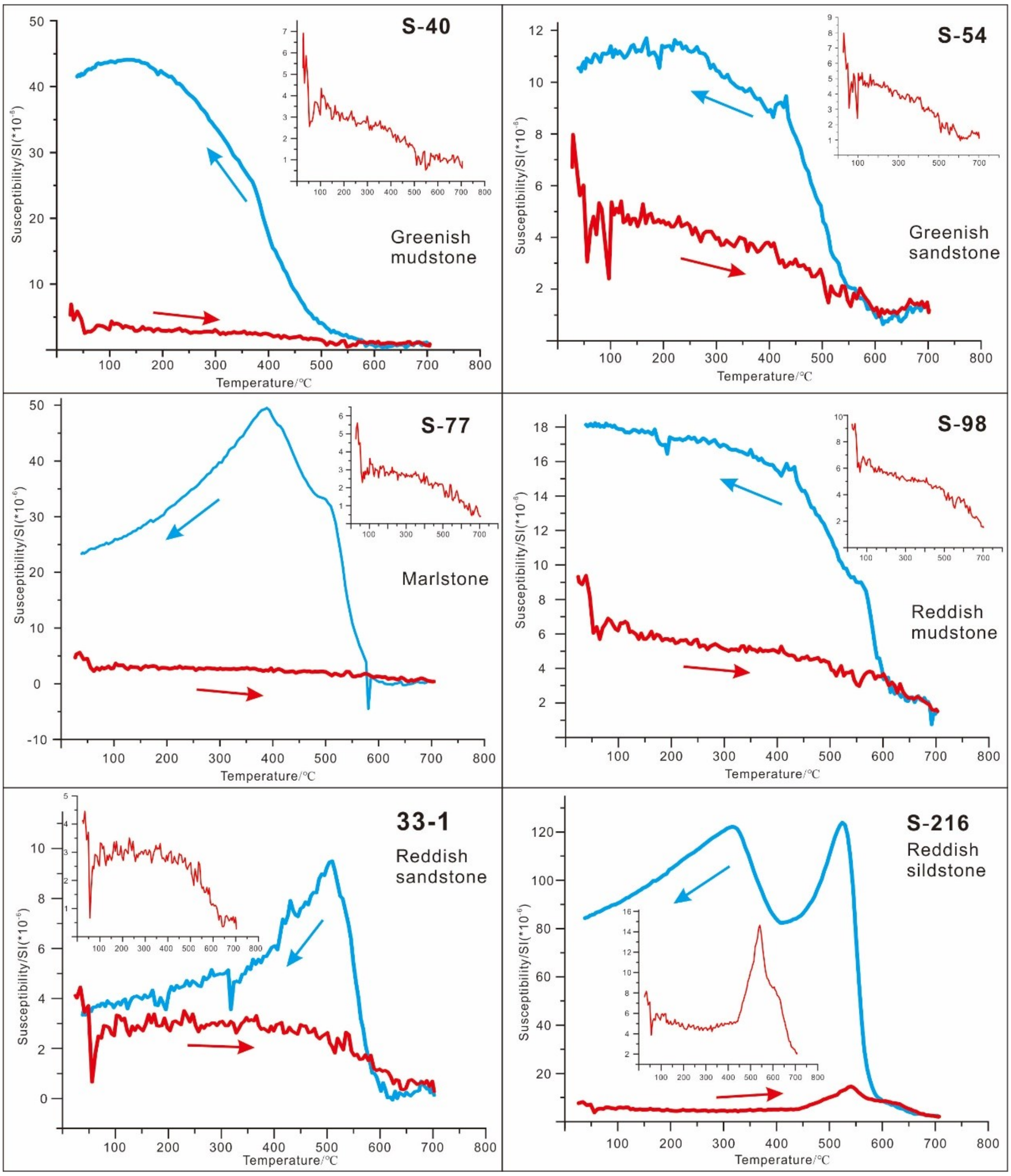

Figure S4. K-T curves of representative specimens.

3. U-Pb geochronology methods and results

Methods

Zircons were separated from a ~1 cm thick ash bed in the middle part of the Sunjiagou Formation at the SCH section (Fig. S1 and S2). After pulverization using a shatterbox, heavy minerals were separated using standard magnetic and high-density liquid separation techniques; several hundred zircon grains were obtained from the > 2,000 g sample. At least 200 zircon grains were selected, which were mounted in epoxy resin and polished down to expose their internal structures for subsequent cath-odoluminescence (CL) imaging.

The U–Pb isotopic and trace element analyses of zircons were conducted at the Mineral Rock Laboratory in Hubei Province, Geological Experimental Testing Center, using a Agilent 7700X inductively coupled plasma mass spectrometer (ICP-MS) coupled to a Geolas Pro laser ablation system. For detailed methods refer to Liu et al. (2008). Zircon was ablated with a laser beam of 32 μm-diameter. Offline data selection, integration of background and analyte signals, time-drift corrections, and quantitative calibrations of the raw U–Pb and trace element data were analyzed through ICPMSDataCal (Liu et al., 2010). Age interpretations are based on $^{206}Pb/^{238}U$ dates. Errors are at 1σ analytical uncertainty.

Eight prismatic and multifaceted zircon grains (some with axial glass inclusions) were selected under binocular microscope and were analyzed by the U-Pb CA-ID-TIMS method at the Massachusetts Institute of Technology (MIT) Isotope Laboratory, USA, following the general analytical procedures described in Ramezani et al. (2011). The selected zircons were pre-treated by a chemical abrasion technique modified after Mattinson (2005), which involved thermal annealing at 900°C for 60 hours and partial dissolution in 28M HF inside hydrothermal vessels at 210°C for 12 hours, in order to mitigate the effects of radiation-induced Pb loss. Thoroughly fluxed and rinsed grain were then spiked with the EARTHTIME ET535 mixed ^{205}Pb–^{233}U–^{235}U tracer (Condon et al., 2015; McLean et al., 2015), before complete dissolution in HF for 48 hours followed by an anion-exchange column chemistry for purification of Pb and U. Measurement of the Pb and U isotopes were carried out on a VG Sector 54 multi-collector mass spectrometers equipped with Daly ion-counting systems at MIT.

Isotopic data reduction, date calculation and error propagation used the applications Tripoli and ET_Redux and their algorithms (Bowring et al., 2011; McLean et al., 2011). Complete U-Pb isotopic data are given in Supplementary Data C. All analyses were corrected for initial ^{230}Th disequilibrium using a value of 2.8 as the best estimate for the Th/U ratio of the parent magma. The ash bed age is calculated based on the weighted mean $^{206}Pb/^{238}U$ date of zircons after excluding outlier analyses. The age uncertainty is reported at a 95% confidence interval and in the format ±x/y/z Ma, where x is the analytical (internal) uncertainty only, y includes the additional tracer calibration error and z includes the latter as well as the ^{238}U decay constant error of Jaffey et al. (1971). In order to compare the calculated age with those from other ID-TIMS U-Pb laboratories not using the EARTHTIME tracer (or from other U-Pb techniques), the ±y for either set of data must be taken into account.

Results

The LA-ICP-MS method is firstly employed to constrain the age distribution of the ash bed. Fifteen grains from forty analyzed zircons by LA-ICP-MS show ages ranging from 263±2.7 Ma to 249±2.5 Ma (Fig. S5; Supplementary data C). Subsequently, eight zircons were analyzed by CA-ID-TIMS at MIT, which yielded a weighted mean age of 252.25±0.15 Ma (n=4), as well as four significantly younger Jurassic and Cretaceous ages (Supplementary data C). These data are rejected in this study because: 1) fresh ashes were sampled very carefully in the field, which were collected after digging and removing of superficial sediments; 2) the youngest strata exposed within the studied section is late Triassic, which means that those younger ages are unlikely to be contamination from younger detritus in the outcrops; 3) the LA-ICP-MS results provide maximum depositional ages with a wide range, no dates younger than ~240 Ma are found. Therefore, the Jurassic and Cretaceous ages are in conflict with this evidence and were not used.

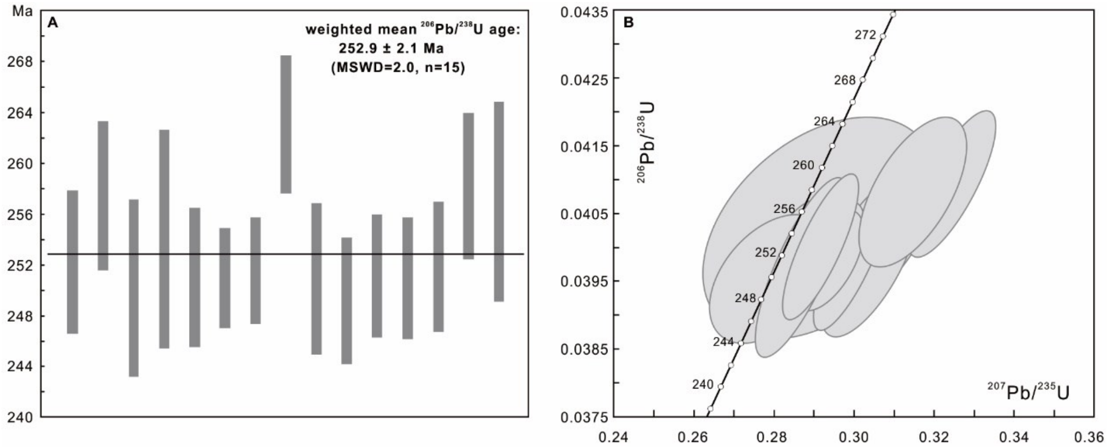

Figure S5. U-Pb dating results for zircons analyzed by LA-ICP-MS.

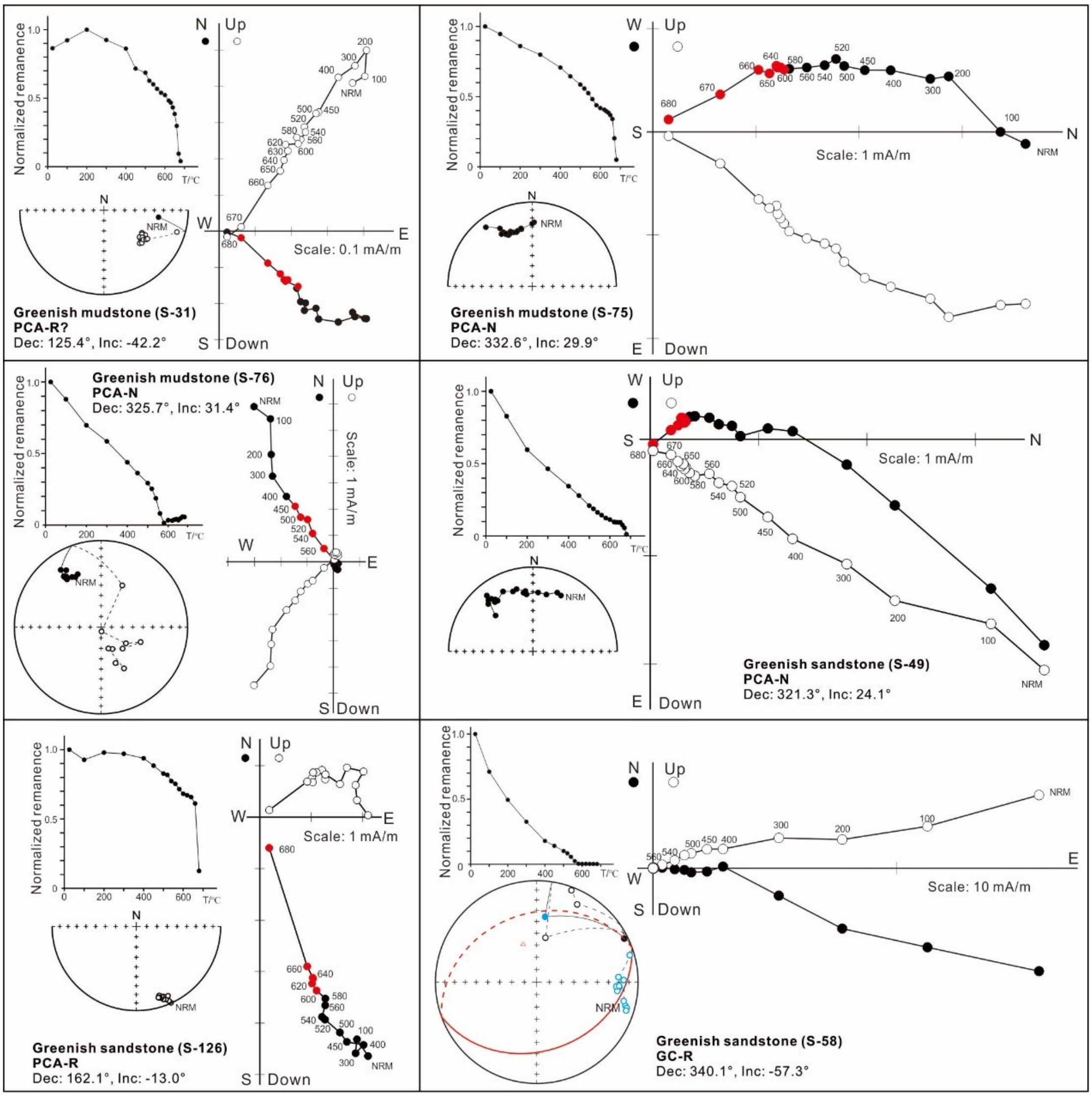

Fig S6. Demagnetization behaviors of greenish mudstone and sandstone specimens, Sunjiagou Formation.

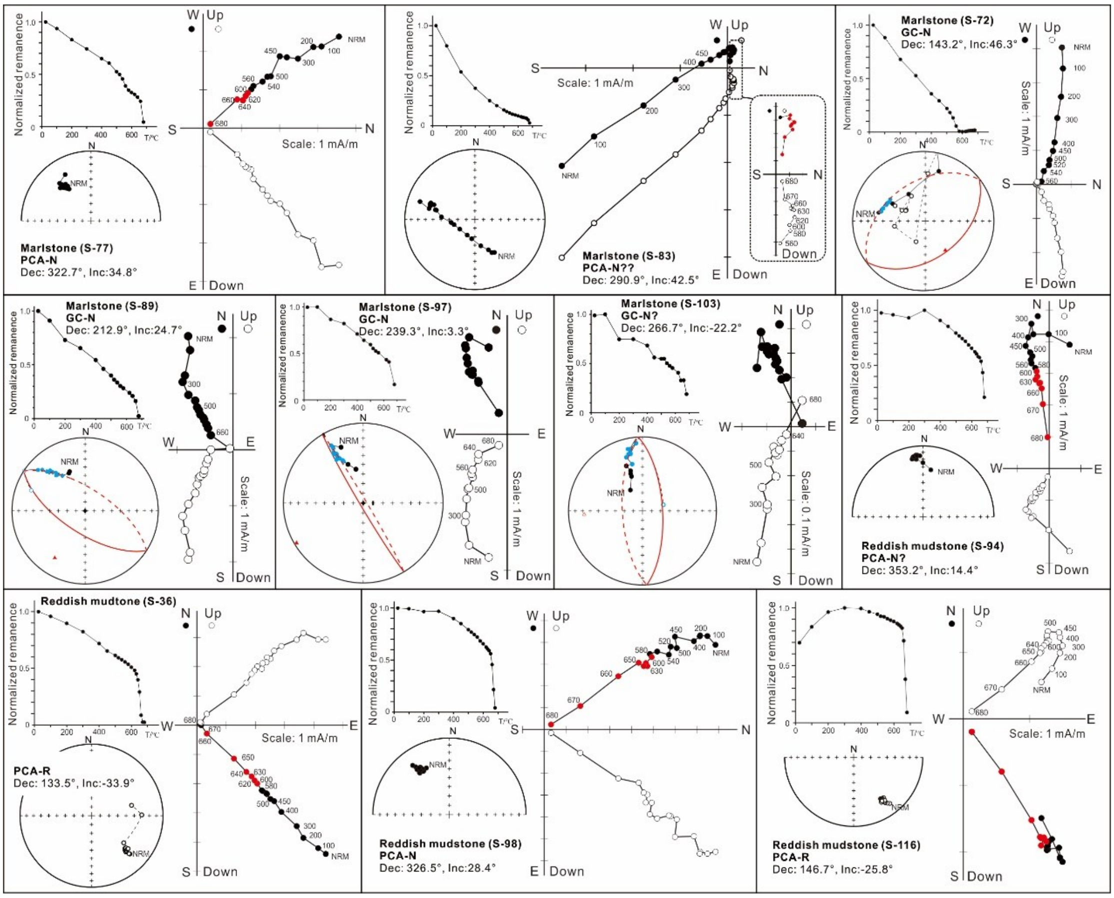

Fig S7. Demagnetization behavior of marlstone and red mudstone specimens, Sunjiagou Formation.

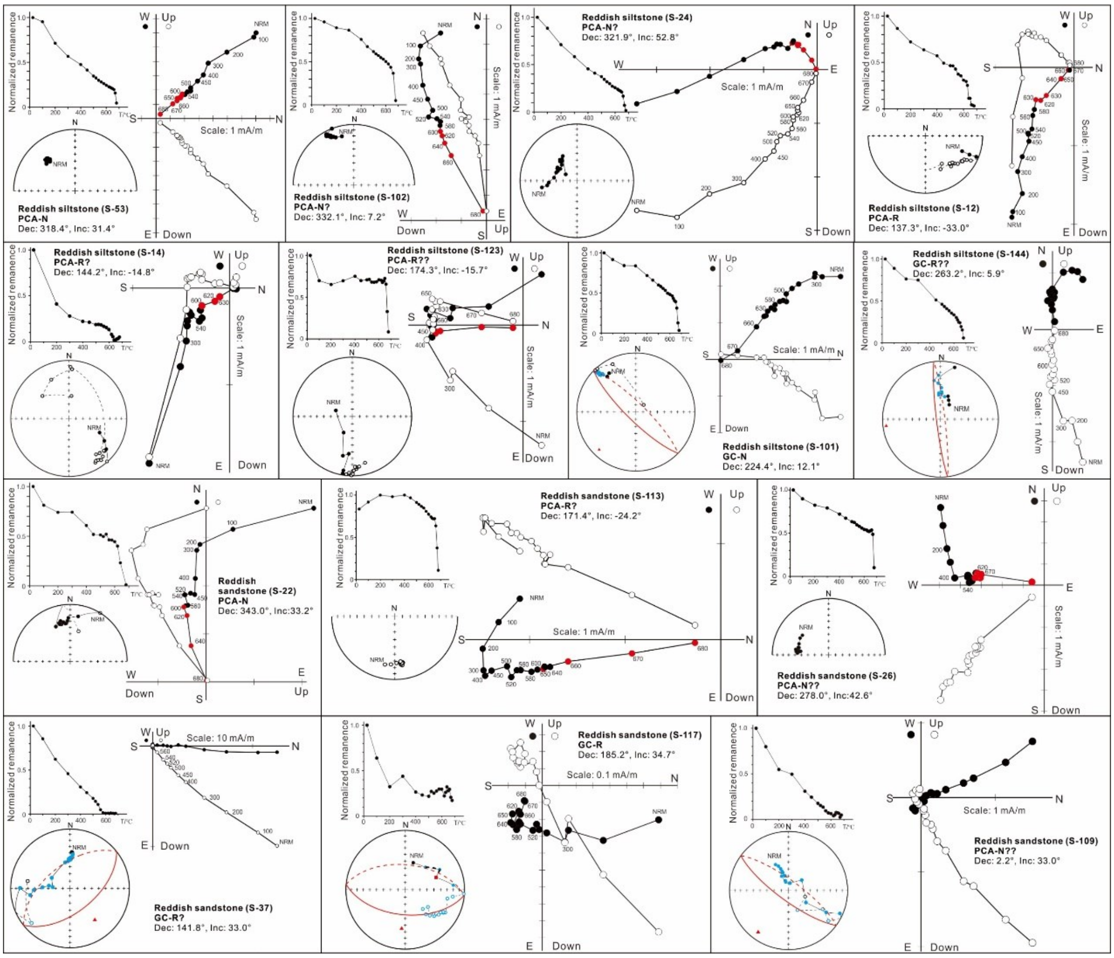

Fig S8. Demagnetization behavior of red siltstone and sandstone specimens, Sunjiagou Formation.

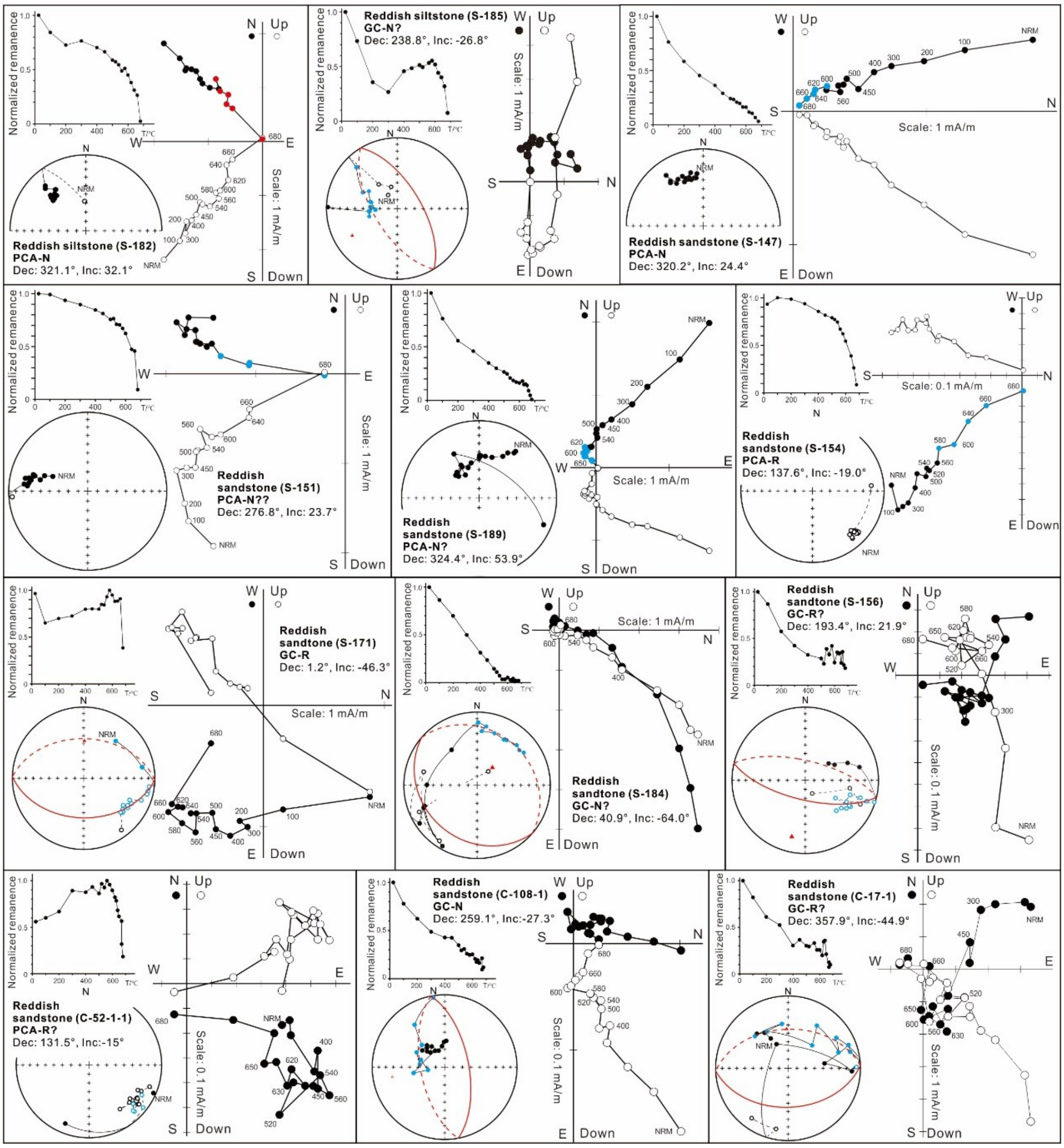

Fig S9. Demagnetization behaviors of red siltstone and sandstone specimens, Liujiagou Formation.

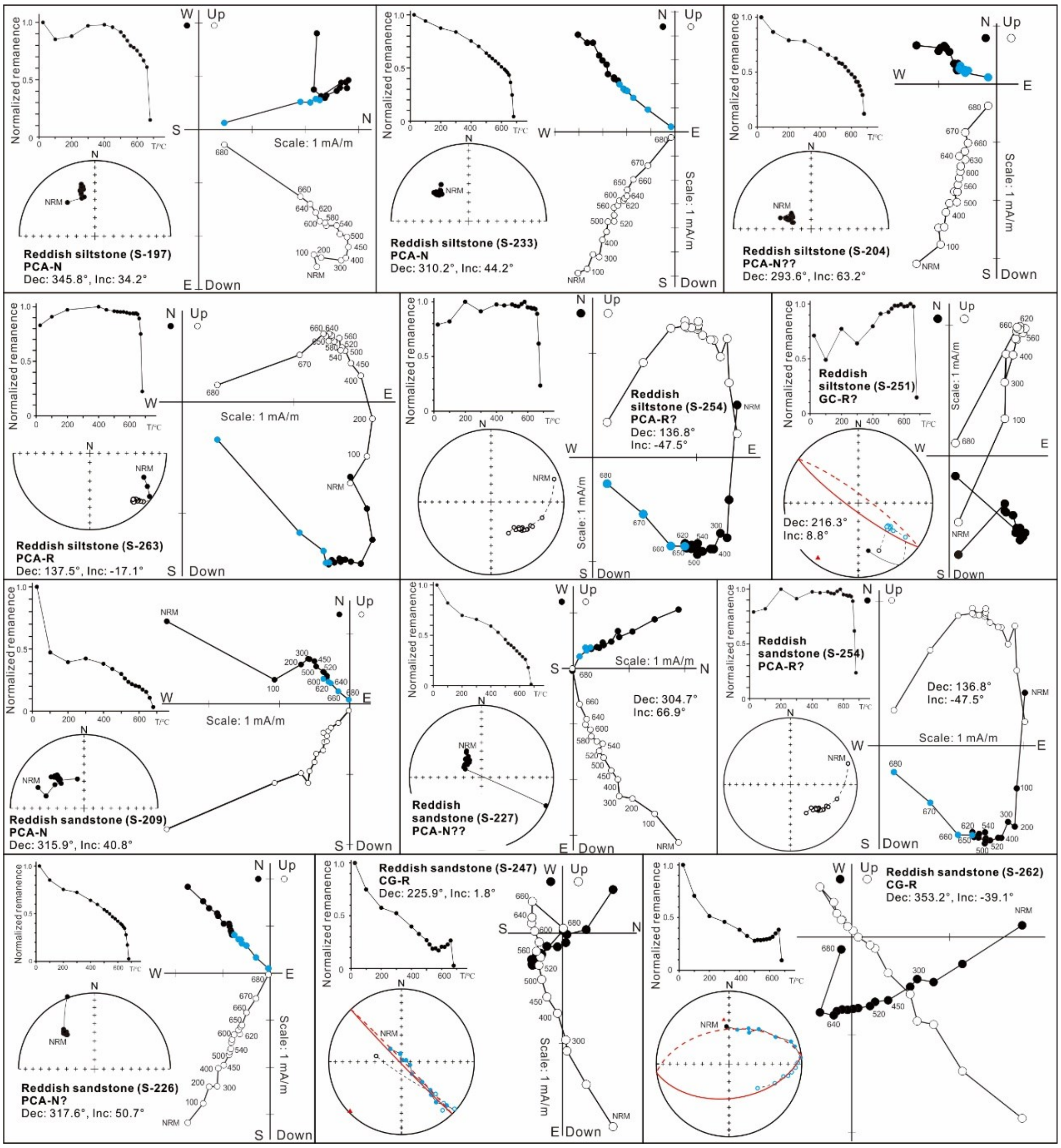

Fig S10. Demagnetization behavior of specimens with red-colored lithologies, Heshanggou Formation.

Table S1. Mean directions, reversal test and virtual geomagnetic poles (VGP) for samples with different directional quality-ratings. Ds, Is, Ks and α_{95} are declination, inclination Fisher dispersion and the 95% confidence cone in stratigraphic coordinates. (s/t) in polarity column are specimens in the set and total in the set. Go, Gc are observed and critical angle for the McFadden & McEhinney (1990) reversal test and the pass categories (Ra, Rb, Rc). Give site latitude and longitude here.

Mean direction (°) of different demagnetization behaviours

SCH		Mean site direction (°)					Reversal test	Virtual Geomagnetic Pole (VGP) (°)			
		Polarity	D_s	I_s	K_s	α_{95}	(G_o/G_c)	Lat.	Long.	δp/δm	Paleolat.
Line fits (142/256)	S1(77/142)	N(59/77)	326.3	32.4	39.96	3.0	Rb (5.86/6.05)*				
		R(18/77)	147.1	-26.6	45.51	5.3					
		N+R	325.6	31.1	39.76	2.6	Rb (5.81/6.05)*	55.0	356.1	1.62/2.90	16.7 N
	S2(47/142)	N(34/47)	322.8	36.9	17.14	6.1	Rc (6.2/11.43)*				
		R(13/47)	145.4	-31.1	18.61	9.9					
		N+R	323.5	35.3	17.54	5.1	Rc (6.2/11.43)*	54.3	2.8	3.41/5.9	19.4 N
	S3(18/142)										
GC fit (95/256)	T1(30/95)	N(8)+R(22)	325.2	34.5	66.70	3.2	Rb (3.97/8.92)	55.3	0.5	2.14/3.72	18.9 N
		Combined S1+T1	326.2	32.2	22.4	2.1	Ra (0.56/4.68)*	55.2	357.4	1.31/2.33	17.4 N
	T2(43/95)	N(17)+R(26)	325.4	35.5	22.45	4.7	Rb (2.97/9.71)	55.9	1.3	3.15/5.44	19.6 N
		Combined S1+T1	324.7	35.1	10.0	3.4	Rb (3.6/7.97)*	55.2	1.5	2.28/3.95	19.3 N
	T3(22/95)										

* used a common K value

4. References

Bowring, J.F., McLean, N.M., Bowring, S.A., 2011. Engineering cyber infrastructure for U-Pb geochronology: Tripoli and U-Pb_Redux. Geochemistry, Geophysics, Geosystems 12, Q0AA19, doi:10.1029/2010GC003479.

Chu, D.L., Tong, J.N., Benton, M.J., Yu, J.X., Huang, Y.F., 2019. Mixed continental-marine biotas following the Permian–Triassic mass extinction in South and North China. Palaeogeography, Palaeoclimatology, Palaeoecology 519, 95-107. https://doi.org/10.1016/j.palaeo.2017.10.028.

Condon, D.J., Schoene, B., McLean, N.M., Bowring, S.A., Parrish, R.R., 2015. Metrology and traceability of U–Pb isotope dilution geochronology (EARTHTIME Tracer Calibration Part I). Geochimica et Cosmochimica Acta 164, 464–480. https://doi.org/10.1016/j.gca.2015.05.026.

De Boer, C.B., and Dekkers, M.J., 1998. Thermomagnetic behaviour of haematite and goethite as a function of grain size in various non-saturating magnetic fields. Geophysical Journal International, 133, 541–552. https://doi.org/10.1046/j.1365-246X.1998.00522.x.

Deng, C., Zhu, R., Jackson, M.J., Verosub, K.L., Singer, M.J., 2001. Variability of the temperaturedependent susceptibility of the Holocene eolian deposits in the Chinese loess plateau: a pedogenesis indicator. Physics and Chemistry of the Earth, Part A: Solid Earth and Geodesy, 26: 873-878. https://doi.org/10.1016/S1464-1895(01)00135-1.

Guo, W.W., Tong, J.N., Tian, L., Chu, D.L., Bottjer, D.J., Shu, W.C., Ji, K.X., 2019. Secular variations of ichnofossils from the terrestrial Late Permian–Middle Triassic succession at the Shichuanhe section in Shaanxi Province, North China. Global and Planetary Change 181, 102978. https://doi.org/10.1016/j.gloplacha.2019.102978.

Jaffey, A.H., Flynn, K.F., Glendenin, L.E., Bentley, W.C., Essling, A.M., 1971. Precision measurement of half-lives and specific activities of ^{235}U and ^{238}U. Physical review C 4, 1889–1906. DOI: https://doi.org/10.1103/PhysRevC.4.1889.

Jiang, Z., Liu, Q., Zhao, X., Jin, C., Liu, C. and Li, S., 2015. Thermal magnetic behaviour of Al-substituted haematite mixed with clay minerals and its geological significance. Geophysical Journal International, 200, 130–143. https://doi.org/10.1093/gji/ggu377**.**

Liu, Y.S., Hu, Z.C., Gao, S., Günther, D., Xu, J., Gao, C.G., Chen, H.H., 2008. In situ analysis of major and trace elements of anhydrous minerals by LA-ICP-MS without applying an internal standard. Chemical Geology 257, 34–43.

Liu, Y.S., Hu, Z.C., Zong, K.Q., Gao, C.G., Gao, S., Xu, J., Chen, H.H., 2010. Reappraisement and refinement of zircon U-Pb isotope and trace element analyses by LA-ICP-MS. Chinese Science Bulletin 55, 1535–1546.

Mattinson, J.M., 2005. Zircon U–Pb chemical abrasion (“CA-TIMS”) method: Combined annealing and multi-step partial dissolution analysis for improved precision and accuracy of zircon ages. Chemical Geology 220, 47–66. https://doi.org/10.1016/j.chemgeo.2005.03.011.

McFadden, P.L., McElhinny, M.W., 1990. Classification of the reversal test in paleomagnetism. Geophysical Journal International 103, 725-729.

McLean, N.M., Bowring, J.F., Bowring, S.A., 2011. An algorithm for U-Pb isotope dilution data reduction and uncertainty propagation. Geochemistry, Geophysics, Geosystems 12, Q0AA18, doi:10.1029/2010GC003478.

McLean, N.M., Condon, D.J., Schoene, B., Bowring, S.A., 2015. Evaluating uncertainties in the calibration of isotopic reference materials and multi-element isotopic tracers (EARTHTIME Tracer Calibration Part II). Geochimica et Cosmochimica Acta 164, 481–501. https://doi.org/10.1016/j.gca.2015.02.040.

Ramezani, J., Hoke, G.D., Fastovsky, D.E., Bowring, A.S., Therrien, F., Dworkin, S.I., Atchley, S.C., Nordt, L.C., 2011. High-precision U-Pb zircon geochronology of the Late Triassic Chinle Formation, Petrified Forest National Park (Arizona, USA): Temporal constraints on the early evolution of dinosaurs. GSA Bulletin 123: 2142–2159. https://doi.org/10.1130/B30433.1.

Yu, Y.Y., Tian, L., Chu, D.L., Song, H.Y., Guo, W.W., Tong, J.N., 2022. Latest Permian–Early Triassic paleoclimatic reconstruction by sedimentary and isotopic analyses of paleosols from the Shichuanhe section in central North China Basin[J]. Palaeogeography, Palaeoclimatology, Palaeoecology, 110726.